R. & M. No. 3031
(17,517)
A.R.C. Technical Report

MINISTRY OF SUPPLY

AERONAUTICAL RESEARCH COUNCIL
REPORTS AND MEMORANDA

Experimental and Theoretical Investigations of the Flow of Air through Two Single-Stage Compressors

By

J. H. HORLOCK,
Engineering Department, Cambridge University

LONDON: HER MAJESTY'S STATIONERY OFFICE
1957
PRICE 10s 6d NET

Experimental and Theoretical Investigations of the Flow of Air through Two Single-Stage Compressors

By

J. H. Horlock,
Engineering Department, Cambridge University

Reports and Memoranda No. 3031
March, 1955

Introduction.—The development of actuator-disc theory and its application to predict the flow through axial-flow turbo-machines has been given in Ref. 1. An investigation of the accuracy of these theoretical predictions of performance has been made on an axial-flow–compressor test rig in the Cambridge University Engineering Laboratories.

This investigation has involved the traversing of pressure and angle measuring instruments at the trailing edge and further downstream of blade rows, and comparisons of the axial velocity profiles obtained from these pressures and yaw angles at the various stations with theoretically predicted profiles.

The changes in the axial velocity profiles at the trailing edges of blade rows due to the interference effect of neighbouring rows have also been studied, both in the stalled and unstalled regions of operation.

1. *Theory.*—The basis of the theory developed in Ref. 1 is the replacement of the blade row by an infinitely thin actuator disc across which there is a sudden change in tangential velocity and vorticity.

Consideration of the equations of motion on either side of the disc shows that there is a perturbation velocity superimposed upon the upstream and downstream infinity values of axial velocity (C_{x1}, C_{x2}) in the neighbourhood of the disc, and that this perturbation varies approximately exponentially in the axial direction.

Thus the perturbation axial velocity C_x' at any distance x from the actuator disc is given by $\{(C_{x2} - C_{x1})/2\}\{\exp(-kx)\}$, where k is an attenuation constant obtained from the first term of the solution of a Bessel-type differential equation (*see* equation 7, Appendix I, Ref. 1).

The flow through several blade rows is obtained by superimposing the sheets of tangential vorticity associated with the actuator discs replacing the various blade rows.

In Ref. 1, methods of calculation were developed based upon two positions of the actuator disc : the trailing edge, and an arbitrary ' centre of pressure ', within the blade row.

Placing the disc within the blade row means that the important interference effect at the trailing edge of any blade row should be that from the row immediately following, and these interference effects are the only ones that may be expected in a compressor with blades of low aspect ratio (blade height/blade spacing), similar to the machine tested.

2. *Experimental Apparatus.*—The axial-flow–compressor test rig presented to the Cambridge University Engineering Laboratory by Rolls-Royce Ltd, and used in these experiments is illustrated diagrammatically in Figs. 1 and 2.

A 25 horse-power, 2,900 r.p.m. induction motor drives the compressor through a step-up gear box. Air is drawn through an annular air-meter and flows past four inlet webs, and through the inlet guide vanes before passing through the compressor.

The compressor may be built in two stages (rotor, stator, rotor, stator), but either of the moving rows and any one or all of the stationary rows (guide vanes or stators) may be removed. A row of outlet straightening vanes is located downstream of the final stator position.

The hub-tip ratio is constant (0·4) through the compressor, and the ratio of blade height to blade axial spacing is 2·1, which is small judged by present day compressor practice for low hub-tip ratio stages. The tip diameter is 14 in. and the tip speed of order 370 ft/sec, with a gear ratio of 2·086 : 1, and 283 ft/sec with a gear ratio of 1·535 : 1.

The motor casing and gearbox are swung to enable torque measurements to be obtained, and equivalent total temperature rises across the compressors to be estimated.

The instrumentation of the compressor is indicated diagrammatically in Fig. 2, which shows the possible traversing planes.

Most of the results detailed in this paper were obtained with a three-hole Fecheimer tube, and other tubes used to check measurements made with this instrument. Details of the calibration of these instruments are given in Ref. 2.

In general, velocity profiles behind stationary rows were obtained by integration of observed values across a complete blade pitch at a given radius, but profiles downstream of rotating rows were based on the mean of five radial traverses, the conditions as recorded by a pressure measuring instrument being substantially uniform along a given circumference.

3. *Experiments.*—Initial tests on the validity of actuator-disc theory were undertaken on a set of compressor blades supplied by Rolls-Royce Ltd. The basis of design of these blades was (*a*) constant axial velocity with radius and (*b*) stator entry-air angle approximately constant with radius. This stage is referred to as the ' Rolls-Royce ' stage. As far as the investigation at Cambridge was concerned the basis of design, necessarily a considerable approximation, was ignored and the compressor stage considered as a direct flow problem in which the variations of air angles at exit from the blade row might be obtained from cascade data[3].

Subsequent investigations were made upon a compressor stage designed on the basis of the model stage of Ref. 1, using Howell's cascade data.

The spacing of the blade rows of each compressor was varied and the changes in performance observed. Such experiments were carried out at several different flows for each compressor.

The experimental results are presented in two sections : ' unstalled ' compressor data for the two types of compressor, and ' stalled ' data.

4. *Compressor Blading Details.*—(*a*) *The Rolls-Royce Stage.*—The Rolls-Royce stage consisted of three rows of blades : a set of stationary inlet guide vanes, a rotating row and a stator row. The details of the blade angles are given in Figs. 3 and 4.

(*b*) *The Model Stage.*—The model stage consisted of one rotor row and one stator row. At design conditions the tangent of outlet angle from the rotor row was required to vary as the radius, and the exit flow from the stator was to be axial. The details of blading designed from Howell's cascade data to fulfil these conditions are given in Figs. 5 and 6. The length/axial spacing ratio was the same as the Rolls-Royce stage ($l/b = 2 \cdot 1$) and the blade chords and axial clearances approximately the same.

5. *Overall Performance Characteristics.*—The overall total pressure and temperature—mass flow characteristics of the two compressor stages are given in Fig. 7. Initial traverses were made at high flows in the unstalled region of the operating range, where the slope of the pressure rise-mass flow curve is negative.

6. *Detailed Traversing of the Rolls Royce Compressor.*—The various compressor arrangements that were traversed in the course of this work are shown diagrammatically in Fig. 8, together with the full two-stage compressor. The terminology used in references to these compressor arrangements is indicated in Fig. 8, and the traversing-plane numbers are given in Fig. 2.

The first test was made on the isolated stationary row, the flow being induced by the second stage rotor, the other rows being removed (G – – R – /G). Next, the first stage rotor was used to study the flow through an isolated rotating row (– R – – –/G). A single-stage build was then traversed in detail, the stage being built up row by row, guide vanes, rotor and stator (G – – R –/G, GR – – –/G, GRS – –/G).

To obtain the ' far upstream ' entry profile, traverses of total pressure, static pressure, were made with a three-hole tube on plane 3 in the absence of the inlet guide vanes (Fig. 8, – R – – –/G) and the axial velocity calculated.

This axial velocity C_{x1} observed in the main stream on plane 3 was higher than the mean axial velocity C_{x0} as calculated from measurements of air-meter static depression on plane 2 (Fig. 2), because of the boundary-layer growth on the annulus walls. The ratio C_{x0}/C_{x1} was found to be 0·980.

All theoretical calculations were based on the assumption that the compressor was running with a uniform entry velocity equal to the observed main stream velocity C_{x1} and at a mean blade speed U_m corresponding to that calculated from observation of motor speed. Thus in any experiment at a specified flow coefficient C_{x1}/U_m the motor speed was first measured and estimated. The required C_{x1} was obtained by setting the entry velocity C_{x0} to a value $0{\cdot}980C_{x1}$. In practice the speed of the induction motor was found to be substantially constant for different compressor builds at a chosen flow coefficient†.

(*a*) *The Isolated Stationary Row* (G – – R –/G, *Fig.* 8. $C_{x1}/U_m = 0{\cdot}670$).—The upstream warping of the entry profile due to the presence of the guide vanes is illustrated in Fig. 9, the result of a traverse on plane 3 (G – – R –/G, 3). Velocities based on integrated total and static pressures obtained on planes 4 and 5 are also shown. Axial velocities are plotted against non-dimensional radius R $\left(\frac{\text{radius}}{\text{tip radius}}\right)$.

The corresponding predicted profiles obtained from actuator-disc theory, the disc being located at the centre-line of the blade, are also shown. The theoretical solutions are based upon a uniform upstream profile and air outlet angles obtained from Howell's cascade data.

The changes in axial-velocity profile from far upstream to the leading edge, and from the trailing edge to far downstream are accurately predicted by the theory.

---

†The ratio $C_{x0}/C_{x1} = 0{\cdot}980$, calculated from observations of velocity on planes 2 and 3, enables an estimate of entry displacement thickness to be made. If the displacement thicknesses are assumed to be the same at hub and tip ($\delta_h^* = \delta_t^* = \delta^*$, then :

$$2\pi\int_{r_h}^{r_t} C_{x0}\, r\, dr = 2\pi\int_{r_h+\delta^*}^{r_t-\delta^*} C_{x1}\, r\, dr$$

$$\delta^* = \left(1 - \frac{C_{x0}}{C_{x1}}\right)\frac{(r_t - r_h)}{2} = 0{\cdot}042 \text{ in.}$$

This compares with a displacement thickness $\delta_t^* = 0{\cdot}050$ in. measured in the course of later work.

(*b*) *The Isolated Rotating Row* (– R – – –/G, *Fig.* 2. $C_{x1}/U_m = 0{\cdot}670$). Traverses upstream and downstream of the rotating row reveal further agreement between the actuator-disc theory and experiment (Fig. 10). It is now of interest to note that the warping of the axial-velocity profile immediately upstream of the blade row is of a different nature to that ahead of the stationary row, the axial velocity increasing towards the tip. Once again, the downstream equilibrium profile is not attained immediately at the trailing edge.

The predictions of actuator-disc theory (discs at blade centre-lines) using the two-dimensional cascade data to predict the air outlet angles, and assuming a uniform upstream profile, are also shown.

The three-hole tube was again used in obtaining these profiles but a check was made using the Conrad yaw-meter and the experimental results are also plotted in Fig. 10, confirming the accuracy of the observations.

(*c*) *The Single-Stage Compressor—Decay Effects.* ($C_{x1}/U_m = 0{\cdot}670$).—The validity of the actuator-disc theory being established for isolated moving and stationary rows, an investigation was made on a single stage.

The single-stage compressor was built up row by row (Fig. 8), traverses being made after each row at the trailing edge and further downstream, before the following row was brought up to the normal adjacent position. The changes in profile (trailing edge to ' downstream infinity ') with no interference effect from the following rows are termed decay effects, and are compared with predicted profiles in Figs. 11 and 12.

It is clear that the ' downstream infinity ' values are not obtained at the trailing edge and it is of interest to note that downstream of the inlet guide vanes and the rotor the axial velocity profiles tend to move further away from the uniform entry profile. Downstream of the stator row, however, the profile if anything tends to flatten, as predicted by the theory using the air angles obtained from two-dimensional cascade data, and assuming a uniform upstream profile (the location of the actuator planes being at the blade centre-lines).

The simplifying assumption of a uniform profile upstream of the guide vanes used in the theoretical calculations leads to the ' concave ' profiles shown for the stator trailing-edge and ' downstream infinity ' axial velocities. Although these calculations show the trend of the flow, it is clear that the high values of axial velocity predicted at the walls are not attained and that boundary-layer corrections should be incorporated if more accurate prediction of the flow is to be made after the first three rows. Errors are cumulative and the accuracy of prediction decreases as the number of blade rows in the compressor arrangement tested is increased.

(*d*) *The Single-Stage Compressor—Interference Effects.* ($C_{x1}/U_m = 0{\cdot}670$). The upstream effects of an adjacent blade row upon the axial-velocity profiles at the trailing edges of the inlet guide vanes and the first rotor were investigated by traversing at these positions with and without the following row placed immediately adjacent.

An interference effect of the rotor upon the inlet-guide-vane trailing-edge profile at the flow coefficient of $C_{x1}/U_m = 0{\cdot}670$ (at which all traverses detailed above were made) was not revealed by experiment (Fig. 13). It should be noted that the experimental profiles obtained far downstream of the inlet guide vanes and the rotor are little different, and that the theoretical curves of Fig. 13 confirm that interference effects should be negligible under such conditions.

The effect of the presence of an adjacent following stator row upon the axial velocity at the trailing edge of the upstream rotor is clearly seen and agrees well with the changes predicted by theory (Fig. 14). The upstream effect of the stator is to flatten the rotor trailing-edge profile and to move it further away from the ' equilibrium ' profile.

Air angles observed in these experiments are shown in Figs. 15, 16, and 17, together with the air angles predicted from Howell's cascade data, which were used in the calculations based on actuator-disc theory.

(*e*) *Summary of Results on the Rolls-Royce Stage.*—These experimental results generally confirm the predictions of the actuator-disc theory.

It is of interest to note the general effects predicted by the actuator-disc theory, based on discs located at the centre-lines of the blades. In general compressor practice the tangential vorticities are larger after rotors than after stationary rows. When the discs are located on the blade centre-lines, the main interference effect to be considered at any trailing edge is that from the row immediately following. This interference effect should steepen the profiles at the trailing edges of stationary rows and flatten the profiles at the rotor trailing edges. It should be noted from the experiments, that downstream of the isolated moving row the equilibrium profile is attained as quickly as in the isolated stationary-row experiment (sections 6(*a*) and (6*b*). Figs. 9 and 10). It is the effect of the following stator which changes the profile away from the equilibrium shape (section 6(*d*). Fig. 14).

In compressors in which the tangential vorticities are greater after the stationary rows the reverse effect should be found, *i.e.*, interference effects should steepen the profile at exit from the rotor, but flatten the axial velocity at exit from the stator. Such compressors are not common, although the model compressor stage of Ref. 1 is an example of this type, and experiments were therefore undertaken on this type of compressor stage to confirm the predictions of the actuator-disc theory.

7. *Detailed Traversing of the Model Stage.*—The two compressor arrangements tested in this series of experiments are shown diagrammatically in Fig. 18. First the changes in axial-velocity profiles through the isolated rotor were investigated and then the modifications to the flow produced by the presence of the stator row adjacent to the rotor were noted.

(*a*) *The Isolated Rotating Row.* ($C_{x1}/U_m = 0{\cdot}720$).—The profile upstream of the rotor in build (– R – – –/G) was observed to be uniform on plane 3 but traverses on plane 4 showed the upstream effect of the rotor (Fig. 19). The steep gradient of axial velocity with radius downstream of the row was not attained immediately at the trailing edge (plane 5) but appeared to be fully developed on plane 8. Similarly the decay effects downstream of the stator in build (– RS – –/G) are seen in Fig. 19 which shows traverses on planes 6 to 8. The calculations of Ref. 1 are shown in Fig. 20 for comparison with the observed velocities (*N.B.* The actuator discs were placed at a plane one-third of the blade chord from the leading edge in the calculations of Ref. 1).

(*b*) *Interference Effects.* ($C_{x1}/U_m = 0{\cdot}720$).—Traverses upstream of the rotor in build (– RS – –/G) showed no change from those observed in build (– R – – –/G), but the axial velocity at the trailing edge of the row was steepened considerably by the presence of the stator row (Fig. 21), as predicted by calculations.

Here it should be noted that the presence of the following stator serves to make the profile approach more closely the radial equilibrium ' infinity ' velocity observed on plane 8 of build (– R – – –/G), the opposite effect to that observed in the series of experiments on the Rolls-Royce stage. However, both types of interference effect are predicted by the actuator-disc analysis.

The experiments on the model stage were repeated at a lower flow and the same overall effects were observed (Figs. 22 to 24). The theoretical calculations at this flow condition, $C_{x1}/U_m = 0{\cdot}585$, are also shown, it being assumed that the air exit angles from the rows were as designed and the flow was reversible. The observed air angles relative to the rotor and stator are shown in Fig. 25. The design angles were achieved closely on the rotor at design flow, but underturning by the stator row is evident. Exit angles on both rotor and stator increased at the lower flow coefficient.

8. *Investigation of Stalled Flow Conditions.*—Overall characteristics of the Rolls-Royce type single-stage compressor built with different blade axial spacings showed identical performance in the unstalled region where the slope of the pressure rise mass flow characteristic was negative, but the differing performance in the stalled region suggested that interference effects were important in this operating region (Fig. 26).

General measurements of the total pressure and yaw angle showed that the flattening of the pressure characteristic was associated with stalling of the stator root and the flattening of the temperature rise characteristic with stalling of the rotor tip.

Complete investigations of the decay and interference effects were made on the Rolls-Royce compressor at two ratios of entry main-stream axial velocity to blade speed at mean radius, $C_{x1}/U_m = 0{\cdot}413, 0{\cdot}289$, similar to the experiments in the unstalled region, made at a flow coefficient $C_{x1}/U_m = 0{\cdot}670$.

All velocities were again obtained by integration of total pressure, static pressure and yaw angle traverses made with a three-hole tube. Conditions as observed with the tube downstream of a rotor were substantially uniform circumferentially, although small variations were observed upstream of an adjacent stalled stator row.

It should be emphasised that the investigations and comparisons described were again limited to the flow outside the wall boundary layers, *i.e.*, between the radial positions $R = \frac{\text{radius}}{\text{tip radius}} = 0{\cdot}48$ and $0{\cdot}92$.

(*a*) *Investigations at a Flow Coefficient* $C_{x1}/U_m = 0{\cdot}413$. *Decay Effects.*—Fig. 27 shows the observed velocity profiles at the trailing edge and far downstream of :

(i) the inlet guide vanes (build G – – R –/G)

(ii) the rotor (build GR – – –/G)

(iii) the stator (build GRS – –/G),

at a flow coefficient $C_{x1}/U_m = 0{\cdot}413$.

Also shown is the warping of the axial-velocity profile upstream of the guide vanes in build (G – – R –/G).

The velocities are plotted in feet per second against non-dimensional radius, $R = \frac{\text{radius}}{\text{tip radius}}$.

Theoretical predictions of performance (Fig. 28) were based on the assumption of uniform velocity upstream equal to C_{x1}. The air outlet angles and total pressure losses of the blade sections were obtained from A. R. Howell's two-dimensional cascade data and the calculated incidence on to the blade section. At very high incidences the curves obtained from Howell were extrapolated (*see* Figs. 29 and 30). The method of calculation has been detailed in Ref. 1, the actuator discs being placed at the blade centre-lines, and a sample calculation is given in Appendix I.

The absolute value of the axial velocities and the general shapes of the profiles are predicted by the theory. The large distortion of the profiles downstream of the rotor (in the compressor arrangement G – – R –/G) has an upstream effect on the axial velocity one chord downstream of the guide-vane trailing edge. This traverse position is no longer the ' downstream infinity ' position, and the observed profile, already warped by the presence of the rotor downstream, is steeper than the calculated ' equilibrium ' profile.

The changes in velocity from the trailing edge of the blade rows to far downstream are again shown to be important.

(*b*) *Interference Effects.*—The axial velocities observed at the inlet guide-vane trailing edge (Fig. 31) are significantly different from the axial velocities measured at the trailing edge in the presence of an adjacent rotor (GR – – –/G), and with the normal compressor arrangement (GRS – –/G). The axial velocity is increased over the major part of the annulus by the presence of the rotor but drops steeply towards the tip of the blade. This corresponds to an increase in

the observed exit air angle from the guide vanes. The flow becomes tangential and there is actually a reversed axial component near the tip. The trend, but not the magnitude, of this interference effect is predicted by actuator-disc analysis based on the blade centre-line positions for the discs.

The major interference effect observed at the trailing edge of the rotor is predicted with considerable accuracy (Fig. 32).

The integrated exit air angles from the three rows are compared in Figs. 15, 16 and 17, with the air angles obtained from Howell's data and used in the calculations.

At a flow coefficient of 0·413 the agreement between observed and predicted is good for the rotor and stator exit air angles. The observed angles downstream of the guide vanes differ considerably from the angles used in the calculations. These angles are assumed invariant with flow coefficient at a given radius, since the incidence on to the guide vanes does not alter with flow. However the angles at the trailing edge of the guide vanes in build (G – – R –/G) agree well with these predicted angles at a flow coefficient of 0·413, and it is clear that the discrepancies observed in builds (GR – – –/G) and (GRS – –/G) are due to the upstream effect of the rotor. Actuator-disc theory assumes that the outlet air angle from a blade row is not affected by the interference from a row downstream, except in so far as the incidence on to the row is changed. The traverses are, however, made not exactly at the trailing edge but approximately 1/6 chord downstream so that there may be changes in axial velocity from the actual trailing edge to the so-called ' trailing-edge traverse position ', and these changes may be considerable. If the tangential velocity remains constant over this axial distance, then since the axial velocity is increasing rapidly at the root and decreasing rapidly at the tip, the observed air angle at the ' trailing-edge traverse position ' will be lower at the root and higher at the tip than the yaw angle at the trailing edge proper. This is the effect that is observed†.

The exit air angles from the rotor suggest that it is uniformly stalled. Analysis on the position of the actuator disc suggests that the disc should be located at an axial plane containing the centre of pressure of the blade row, and that for an unstalled row, the centre-line is a suitable approximation. Under stalled conditions, however, most of the change in tangential velocity is accomplished rapidly near the leading edge of the blading and the centre of pressure moves forward.

The theoretical interference effect due to an actuator disc located at the rotor leading-edge position is shown in Fig. 31, and gives better agreement with the observed velocity at the guide-vane trailing edge (build GR – – –/G), although the steep drop in velocity towards the tip is not predicted.

The stator exit air angles suggest that the stator is not stalled at this flow and the centre-line position for the stator disc may be therefore more nearly correct than a leading-edge location.

(*c*) *Investigations at a Flow Coefficient* $C_{x1}/U_m = 0{\cdot}289$. *The Decay Effect.*—Observed and theoretically predicted profiles (discs at the blade centre-lines) illustrating the decay effect at a flow coefficient of 0·289 are shown in Figs. 33 and 34.

There is a considerable warping of the uniform profile from far upstream to the guide-vane–row leading edge and a large change in axial velocity from the trailing edge to one chord downstream (build G – – R –/G). This latter change is due to the upstream interference effect of the rotor inducing the flow, and the guide vanes can no longer be described as an isolated blade row.

†Another explanation of the change in the air angle at the guide-vane trailing edge may be suggested. The severe interference effects reduce the axial velocity at exit from the guide-vane–row tip until there is in fact a pressure increase across the tip section, and the blade may stall. As there are no cascade data for such conditions, the author was forced to assume the exit air angle was invariant with flow coefficient.

Downstream of the rotor the profiles are quite accurately predicted. In the calculations the steep decrease of axial velocity towards the tip is associated with large losses. The radius at which the axial velocity theoretically becomes zero can be computed only approximately, due to the large variation in loss with incidence under these conditions. It is assumed that the axial velocity is zero from this radius to the tip, and negative velocities are not computed.

The observed flattening of the profile far downstream of the stator is not accurately predicted, although the theoretical trailing-edge velocity profile is of the right order.

There are large variations of static and total pressure, and yaw angle in the circumferential traverses near the stator blade tip, and the integrated results shown give merely a qualitative picture of the flow conditions.

(*d*) *Interference Effects.*—The large observed interference effect at the guide-vane trailing edge (Fig. 35) is suggested by calculations based on the centre-line position of the actuator disc, but the theoretical effect is not as great as that observed.

Theory suggests little interference effect at the rotor trailing edge and this is confirmed by experiment (Fig. 36).

The theoretical and experimental outlet air angles of Figs. 15, 16 and 17 again show the large interference effect of the rotor on the guide-vane outlet air angle in build (GRS – –/G) whereas the exit angles at the trailing edge in build (G – – R– /G) agree quite well with the predicted angles. Once again it is probable that the axial-velocity changes from the actual trailing edge to the ' trailing-edge traverse position ' are responsible for the alterations in outlet air angles.

The exit air angles suggest that the rotor is well stalled all along the blade length, and that the stator tip is stalled, although not as badly as the calculations predict. This discrepancy, due to incorrect incidence calculation, is largely responsible for the inaccuracy in the prediction of the axial-velocity profile far downstream of the stator.

As the rotor and stator are fully and partially stalled respectively, the theoretical calculations were repeated with the rotor and stator actuator discs placed at the leading-edge positions. The axial velocities through the compressor (build GRS – –/G) thus computed are shown in Fig. 37, together with the observed velocities. Agreement is remarkable considering the complicated nature of the flow.

The reversed flow at the guide-vane trailing-edge tip is again noticeable in these traverses. In this condition the velocity becomes very large and predominantly tangential. The compressor wall becomes warm after continual running at this flow. The observed total pressure is above atmospheric pressure, and the recording instrument has to be turned past the tangential position if the yaw-angle balance is to be obtained. Thus the axial-velocity component is in the reverse direction to the main flow, and the air must have recirculated through the rotor. A sketch of the nature of this recirculation is given in Fig. 38, which shows the direction of the axial-velocity components. The reversal of the axial velocity is associated with large tangential velocity.

9. *Overall Performance Prediction.*—Integrated measurements of observed (total pressure $\times$ axial velocity) at exit from the compressor (build GRS – –/G) over the sector of annulus available to the traversing instrument give mean total-pressure rises in good agreement with the usual method of total-pressure–rise calculation (from outlet statics), at the three flow coefficients $C_{x1}/U_m = 0{\cdot}289$, $0{\cdot}413$, $0{\cdot}670$, i.e., $C_{x0}/U_m = 0{\cdot}284$, $0{\cdot}405$, $0{\cdot}656$. These results are shown in Fig. 39.

Calculations from actuator-disc theory of the total temperature rise and the total pressure rise at these three flows are also shown on Fig. 39.

The mean total temperature rise is obtained from :

$$\frac{K_p \Delta T}{U_m^2} = \frac{1}{U_m^2} \frac{\int_{r_h}^{r_t} U\left\{C_{x3e}\left(U - C_{x3e} \tan \beta_{3e}\right) - C_{x2e}^2 \tan \alpha_{2e}\right\} r \, dr}{\int_{r_h}^{r_t} C_{x1} r \, dr \qquad\qquad r \, dr}$$

where U is the blade speed

U_m is the blade speed at the mean radius

C_{x3e} is the predicted axial velocity at the rotor trailing edge

C_{x2e} is the predicted axial velocity at the guide-vane trailing edge

β_{3e} is the exit air angle at the rotor trailing edge (relative)

α_{2e} is the exit air angle at the guide-vane trailing edge

r is the radius

C_{x1} is the entry axial velocity.

The mean total pressure loss is computed from :

$$\frac{\Delta \bar{P}}{\rho U_m^2} = \frac{1}{\rho U_m^2} \frac{\int_{r_h}^{r_t} C_{x2e} (\Delta \bar{P})_R \, r \, dr + \int_{r_h}^{r_t} C_{x3e} (\Delta \bar{P})_S \, r \, dr}{\int_{r_h}^{r_t} C_{x1} r \, dr}$$

where ρ = ambient density

$(\Delta \bar{P})_R$ = rotor total pressure loss (from Howell data)

$(\Delta \bar{P})_S$ = stator total pressure loss (from Howell data).

It is assumed that there are no losses through the guide vanes, so that $\Delta P/\rho U_m^2 = (K_p \Delta T/U_m^2) - (\Delta \bar{P}/\rho U_m^2)$ where ΔP is the total pressure rise across the stage.

At the high unstalled flow the total temperature rise is predicted quite accurately, but the losses are underestimated. It should be remembered that secondary flow losses have not been included.

At the mean flow coefficient $C_{x1}/U_m = 0{\cdot}413$, agreement is again quite good, but at the lowest flow the total temperature rise is underestimated. In the calculations it is assumed that no work is done on the fluid and there are no losses when the axial velocity drops to zero. Thus the work is computed for the fluid outside the recirculation area, and the amount of energy pumped into this standing vortex ring is ignored.

Similar integration of the observed changes in tangential velocity, excluding the part of the annulus where axial velocities are reversed, gives a total temperature rise coefficient $K_p \Delta T/U_m^2$ some 45 per cent of that calculated from the power input to the motor.

Thus it appears that some 55 per cent of the energy supplied is used in maintaining the recirculation vortex, where axial velocities are low and changes in tangential velocity are high. This energy does not all appear as a temperature rise of the main stream but is dissipated as heat loss through the casing.

10. *Conclusions.*—Experimental confirmation of the accuracy of actuator-disc theory has been obtained in the testing of two single-stage compressors operating at several different flow coefficients.

REFERENCES

No.	*Author*	*Title, etc.*
1	J. H. Horlock	Some actuator-disc theories for the flow of air through axial-flow turbo-machines. R. & M. 3030. December, 1952.
2	J. H. Horlock	Instrumentation used in measurement of the three-dimensional flow in an axial-flow compressor. A.R.C. C.P. No. 321.
3	A. R. Howell	The present basis of axial-flow compressor design. Part I. Cascade and theory performance. R. & M. 2095. June, 1942.

APPENDIX I

Sample Actuator-Disc Calculation for Rolls-Royce Compressor Stage. Build (GRS – –/G). (*Discs at Centre-Lines.* $C_{x1}/U_m = 0{\cdot}413$.) A final approximation for the stalled flow conditions of the Rolls-Royce–type stage operating at a flow coefficient of $C_{x1}/U_m = 0{\cdot}413$, is given below.

The entry axial velocity C_{x1} is taken as $1{\cdot}0$, and the blade-tip speed is then $U_{tip} = 3{\cdot}180$. The cascade data of Figs. 29 and 30 are used.

At the rotor tip and stator root there is severe stalling. Under such conditions calculations become difficult as small changes in incidence on to the blade rows result in large changes of the predicted losses. The calculations may give negative values of C_{x3}^2, C_{x4}^2 far downstream of rotor and stator, and it is assumed that these axial velocities far downstream drop to zero but not below zero at these sections.

Velocity triangles for the three blade rows may be drawn thus :

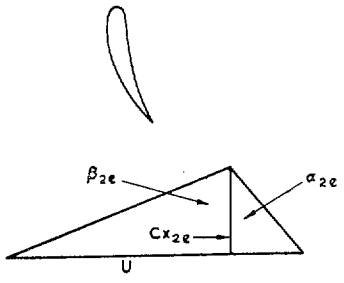

Guide Vanes

Blade exit angle α_2^1

$\alpha_{2e} = \alpha_2^1$ — deviation (δ)

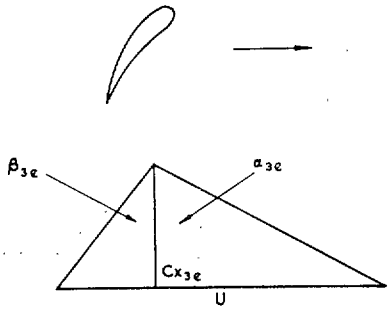

Rotor

Total pressure loss

$$\frac{2\Delta\bar{P}_R}{\rho} = \xi_R W_R^2$$

Entry blade angle β_2^1

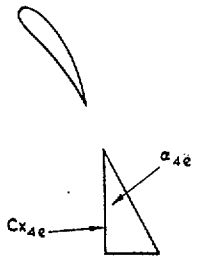

Stator

Total pressure loss

$$\frac{2\Delta\bar{P}_S}{\rho} = \xi_S W_S^2$$

Entry blade angle α_3^1

The method of solution is to take values of the 'infinity' axial velocities, C_{x1}, C_{x2}, C_{x3}, C_{x4} from a previous approximation and to check that arithmetical solutions of the actuator disc equations give values of the axial velocity profiles close to the guessed values.

The calculations given here are the last of six similar approximations.

APPENDIX I—continued

(a) Calculation of Trailing-Edge Velocities C_{x2e}, C_{x3e}, C_{x4e} From Downstream Infinity Velocities of Previous Approximation

R	0·4	0·5	0·6	0·7	0·8	0·9	1·0
C_{x1}	1·0	1·0	1·0	1·0	1·0	1·0	1·0
C_{x2}	1·120	1·100	1·072	1·030	0·985	0·930	0·860
C_{x3}	1·360	1·340	1·280	1·182	0·990	0·785	0·570
C_{x4}	0·284	0·604	0·900	1·100	1·200	1·050	0·700
$0{\cdot}536C_{x2}$	0·600	0·589	0·575	0·551	0·527	0·498	0·460
$0{\cdot}232C_{x1}$	0·232	0·232	0·232	0·232	0·232	0·232	0·232
$0{\cdot}232C_{x3}$	0·316	0·311	0·297	0·274	0·232	0·182	0·113
C_{x2e}	1·148	1·132	1·104	1·057	0·991	0·912	0·824
$0{\cdot}536C_{x3}$	0·729	0·718	0·686	0·634	0·528	0·420	0·268
$0{\cdot}232C_{x4}$	0·066	0·140	0·208	0·256	0·278	0·247	0·162
$0{\cdot}232C_{x2}$	0·260	0·255	0·249	0·239	0·228	0·216	0·200
C_{x3e}	1·055	1·113	1·143	1·129	1·034	0·883	0·667
$0{\cdot}768C_{x4}$	0·218	0·464	0·692	0·845	0·921	0·805	0·538
$0{\cdot}232C_{x3}$	0·316	0·311	0·297	0·274	0·232	0·182	0·113
C_{x4e}	0·534	0·775	0·989	1·119	1·153	0·987	0·657

N.B. $$C_{x2e} = C_{x2} - \frac{(C_{x2} - C_{x1})}{2} e^{-\frac{3\cdot23}{4\cdot2}} + \frac{C_{x3} - C_{x2}}{2} e^{-\frac{3\cdot23}{4\cdot2}}$$

$$= 0{\cdot}536C_{x2} + 0{\cdot}232(C_{x1} + C_{x3})$$

Similarly $$C_{x3e} = 0{\cdot}536C_{x3} + 0{\cdot}232(C_{x2} + C_{x4})$$

$$C_{x4e} = 0{\cdot}768C_{x4} + 0{\cdot}232C_{x3}$$

(*b*) *Calculation of* C_{x2}, *Axial Velocity Far Downstream of Guide Vanes*

$$d(C_{x2})^2 = -\frac{1}{R^2}\, d(RC_{x2e} \tan \alpha_{2e})^2$$

R	0·4	0·5	0·6	0·7	0·8	0·9	1·0
C_{x2e}	1·148	1·132	1·104	1·066	0·988	0·904	0·824
*$\tan \alpha_{2e}$	0·158	0·236	0·313	0·388	0·466	0·550	0·632
$RC_{x2e} \tan \alpha_{2e}$	0·073	0·134	0·207	0·289	0·372	0·447	0·521
$(RC_{x2e} \tan \alpha_{2e})^2$	0·005	0·018	0·043	0·083	0·138	0·199	0·271
$d[RC_{x2e} \tan \alpha_{2e}]^2$		0·013	0·025	0·040	0·055	0·061	0·072
$\frac{1}{R^2}$		4·93	3·31	2·36	1·78	1·39	1·11
$d(C_{x2})^2$		−0·062	−0·082	−0·095	−0·098	−0·085	−0·076
C_{x2}^2	1·299	1·237	1·155	1·060	0·962	0·857	0·781
†C_{x2}	1·140	1·118	1·076	1·030	0·980	0·925	0·885

*From exit blade angle and deviation rule $\delta = 0{\cdot}190\ s/c\,\theta$, where θ = blade camber, s/c = space/chord ratio.

†Checked graphically for continuity, and compared with initial value of C_{x2} in Fig. 40.

(c) *Calculation of C_{x3} Axial Velocity Far Downstream of Rotor*

$$d(C_{x3})^2 = d(C_{x2})^2 + \frac{1}{R^2}\left[d(RC_{x2e}\tan\alpha_{2e})^2 - d\{R^2(U - C_{x3e}\tan\beta_{3e})^2\}\right]$$
$$+ 2d[\Omega\{R(U - C_{x3e}\tan\beta_{3e}) - RC_{x2e}\tan\alpha_{2e}\}] - d[\xi_R W_R^2]$$

R	0·4	0·5	0·6	0·7	0·8	0·9	1·0
C_{x2e}	1·148	1·132	1·104	1·066	0·998	0·904	0·824
$C_{x2e}\tan\alpha_{2e}$	0·181	0·267	0·346	0·413	0·465	0·497	0·521
$U = \Omega R$	1·272	1·590	1·908	2·225	2·545	2·860	3·180
$U - C_{x2e}\tan\alpha_{2e}$	1·091	1·323	1·562	1·812	2·080	2·363	2·659
$\tan\beta_{2e} = \dfrac{U - C_{x2e}\tan\alpha_{2e}}{C_{x2e}}$	0·952	1·170	1·418	1·699	2·085	2·620	3·220
β_{2e}	43·5	49·5	54·8	59·5	64·4	69·1	72·6
β_2^1	25·5	31·9	37·8	43·2	48·1	52·9	57·5
$i_R = \beta_{2e} - \beta_2^1$	18·0	17·6	17·0	16·3	16·2	16·2	15·1
β_{3e} (From Fig. 29)	9·5	21·3	30·9	38·8	46·8	55·3	62·0
ξ_R (From Fig. 29)	0·030	0·030	0·025	0·052	0·100	0·230	0·350

Calculation of C_{x3}—continued

$$d(C_{x3})^2 = -\frac{1}{R^2}\,d\{R^2(U - C_{x3e}\tan\beta_{3e})^2\} - d(\xi_R W_R{}^2) + 2\Omega\, d\{R(U - C_{x3e}\tan\beta_{3e}) - RC_{x2e}\tan\alpha_{2e}\}$$

R	0·4	0·5	0·6	0·7	0·8	0·9	1·0
$\tan\beta_{3e}$	0·167	0·390	0·598	0·803	1·068	1·442	1·880
C_{x3e}	1·055	1·113	1·143	1·129	1·034	0·883	0·667
$C_{x3e}\tan\beta_{3e}$	0·177	0·425	0·684	0·906	1·102	1·275	1·260
$(U - C_{x3e}\tan\beta_{3e})$	1·095	1·165	1·224	1·319	1·443	1·585	1·920
$R(U - C_{x3e}\tan\beta_{3e})$	0·438	0·583	0·735	0·924	1·152	1·428	1·920
$R^2(U - C_{x3e}\tan\beta_{3e})^2$	0·192	0·340	0·540	0·852	1·325	2·030	3·680
$d\{R^2(U - C_{x3e}\tan\beta_{3e})^2\}$		0·148	0·200	0·312	0·473	0·705	1·650
$\frac{1}{R^2}$		4·93	3·31	2·36	1·78	1·39	1·11
$-\frac{1}{R^2}d\{R^2(U - C_{x3e}\tan\beta_{3e})^2\}$		−0·730	−0·662	−0·736	−0·842	−0·980	−1·830
$R(U - C_{x3e}\tan\beta_{3e} - C_{x2e}\tan\alpha_{2e})$	0·366	0·451	0·528	0·635	0·780	0·981	1·400
$d[R(U - C_{x3e}\tan\beta_{3e} - C_{x2e}\tan\alpha_{2e})]$		0·085	0·077	0·107	0·145	0·201	0·419
$x\,2\Omega$		0·540	0·489	0·680	0·923	1·280	2·660
$\xi_R\{C_{x2e}{}^2(1 + \tan^2\beta_{2e})\} = \xi_R W_R{}^2$	0·075	0·090	0·090	0·220	0·528	1·480	2·700
$-d(\xi_R W_R{}^2)$		−0·015	0·000	−0·130	−0·308	−0·952	−1·220
$d(C_{x3})^2$		−0·305	−0·173	−0·186	−0·227	−0·652	−0·390
$C_{x3}{}^2$	2·105	·1800	1·627	1·451	1·214	0·562	(−0·172)
$*C_{x3}$	1·450	1·342	1·280	1·202	1·102	0·752	0·411

*Checked graphically for continuity and compared with initial value of C_{x3} in Fig. 40.

(d) Calculation of C_{x4} Axial Velocity Far Downstream of Stator

$$d(C_{x4})^2 = d(C_{x3})^2 + \tfrac{1}{R^2}\, d\{R^2(U - C_{x3e}\tan\beta_{3e})^2 - R^2C_{x2e}{}^2\tan^2\alpha_{2e}\} - d(\xi_s\, W_s{}^2)$$

R	0·4	0·5	0·6	0·7	0·8	0·9	1·0
$U - C_{x3e}\tan\beta_{3e}$	1·095	1·165	1·224	1·319	1·443	1·585	1·920
$\tan\alpha_{3e} = \dfrac{U - C_{x3e}\tan\beta_{3e}}{C_{x3e}}$	1·031	1·046	1·070	1·170	1·398	1·795	2·880
α_{3e}	45·9	46·3	47·0	49·5	54·5	60·9	70·9
α_3'	28·5	30·25	32·4	34·9	37·6	40·9	44·3
i_s	17·4	16·1	14·6	14·6	16·9	20·0	26·5
α_{4e}	12·0	15·0	18·0	21·8	30·8	42·0	57·0
ξ_s	0·030	0·028	0·025	0·026	0·075	0·250	0·580
$\xi_s C_{x3e}{}^2(1 + \tan^2\alpha_{3e}) = \xi_s W_s{}^2$	0·069	0·073	0·070	0·078	0·266	0·825	0·2410
$-\alpha(\xi_s\, W_s{}^2)$		+0·004	+0·003	−0·008	−0·182	−0·559	−1·585
$d\{R^2(U - C_{x3e}\tan^2\beta_{3e})^2\}$		+0·148	+0·200	+0·312	+0·374	+0·705	+1·650
C_{x4e}	0·534	0·775	0·989	1·119	1·153	0·987	0·670
$\tan\alpha_{4e}$	0·212	0·268	0·324	0·400	0·596	0·901	1·540
$RC_{x4e}\tan\alpha_{4e}$	0·045	0·104	0·193	0·312	0·553	0·800	1·030
$(RC_{x4e}\tan\alpha_{4e})^2$	0·002	0·011	0·037	0·097	0·305	0·640	1·060
$d(RC_{x4e}\tan\alpha_{4e})^2$		0·009	0·026	0·060	0·208	0·335	0·420
$d\{R^2(U - C_{x3e}\tan\beta_{3e})^2 - R^2C_{x4e}{}^2\tan\alpha_{4e}\}$		0·139	0·174	0·252	0·265	0·370	1·230
$\times \dfrac{1}{R^2}$		0·690	0·578	0·595	0·470	0·510	1·360
$C_{x3}{}^2$	1·850	1·790	1·640	1·390	0·980	0·615	0·325
$d(C_{x3}{}^2)$		−0·060	−0·150	−0·250	−0·410	−0·365	−0·290
$d(C_{x4}{}^2)$		+0·626	+0·431	0·335	−0·126	−0·414	−0·515
$C_{x4}{}^2$	(−0·076)	0·550	0·981	0·316	1·190	1·484	1·222
$*C_{x4}$	0	0·743	0·991	1·148	1·092	0·880	0·512

*Checked graphically for continuity and compared with initial value of C_{x4} in Fig. 40.

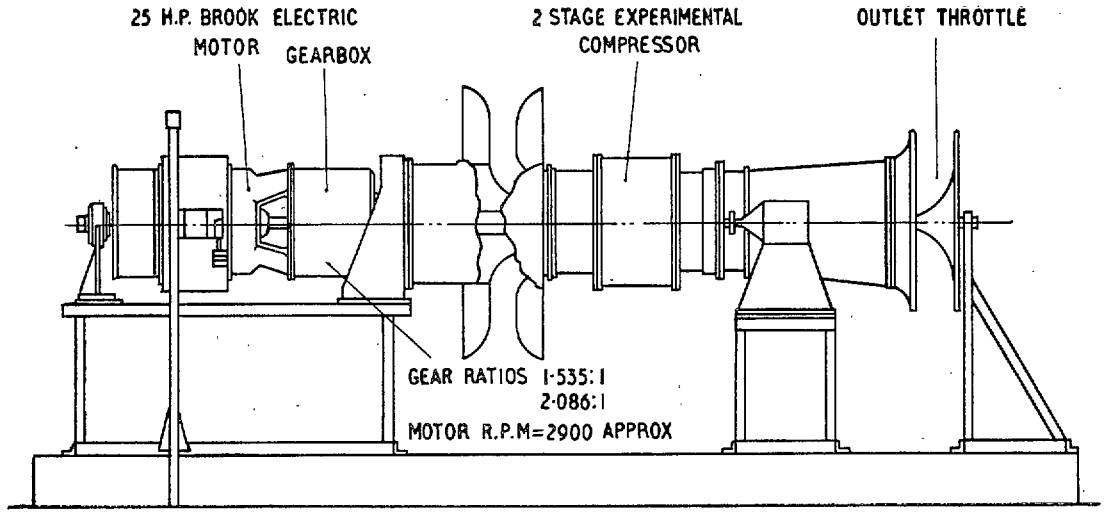

FIG. 1. Diagrammatic lay-out of rig.

PLANE No	ANNULUS AREA	INSTRUMENTATION
P. 1.	369·45 □"	5 STATICS FRONT WALL, 5 STATICS REAR WALL PROVISION FOR TRAVERSING
P. 2.	129·31 □"	3 ADJUSTABLE IMMERSION KIEL PROBES
P. 3.	129·31 □"	3 STATICS OUTER WALL. PROVISION FOR TRAVERSING
P. 4.	129·31 □"	3 STATICS OUTER WALL. PROVISION FOR TRAVERSING
P. 5.	129·31 □"	3 STATICS OUTER WALL. PROVISION FOR TRAVERSING
P. 6.	129·31 □"	3 STATICS OUTER WALL. PROVISION FOR TRAVERSING
P. 7.	129·31 □"	3 STATICS OUTER WALL. PROVISION FOR TRAVERSING
P. 8.	129·31 □"	3 STATICS OUTER WALL. PROVISION FOR TRAVERSING
P. 9.	129·31 □"	5 OUTER WALL STATICS. 5 INNER WALL STATICS. 3 ADJUSTABLE IMMERSION KIEL PROBES.
P. 10.	——	3 STAGNATION THERMOMETER POCKETS.

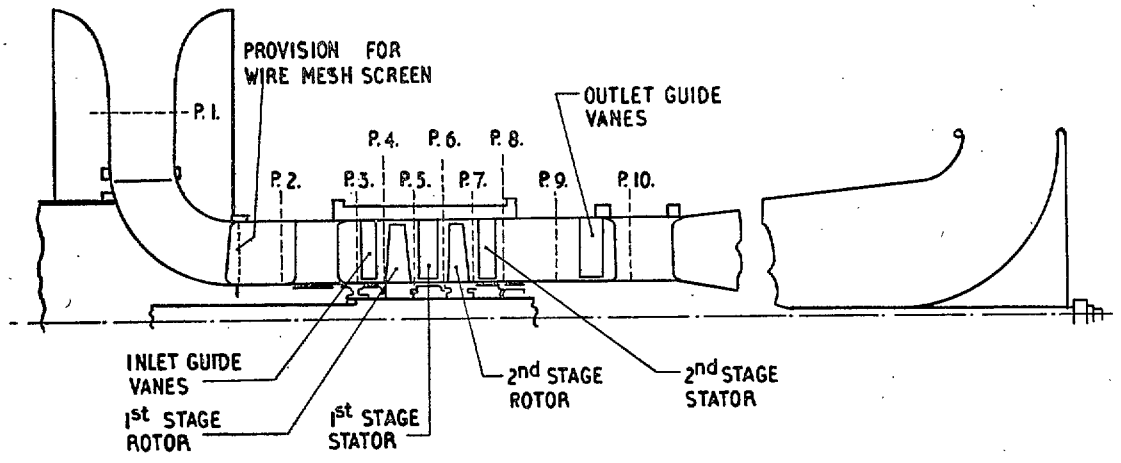

FIG. 2. Two-stage experimental compressor.

B

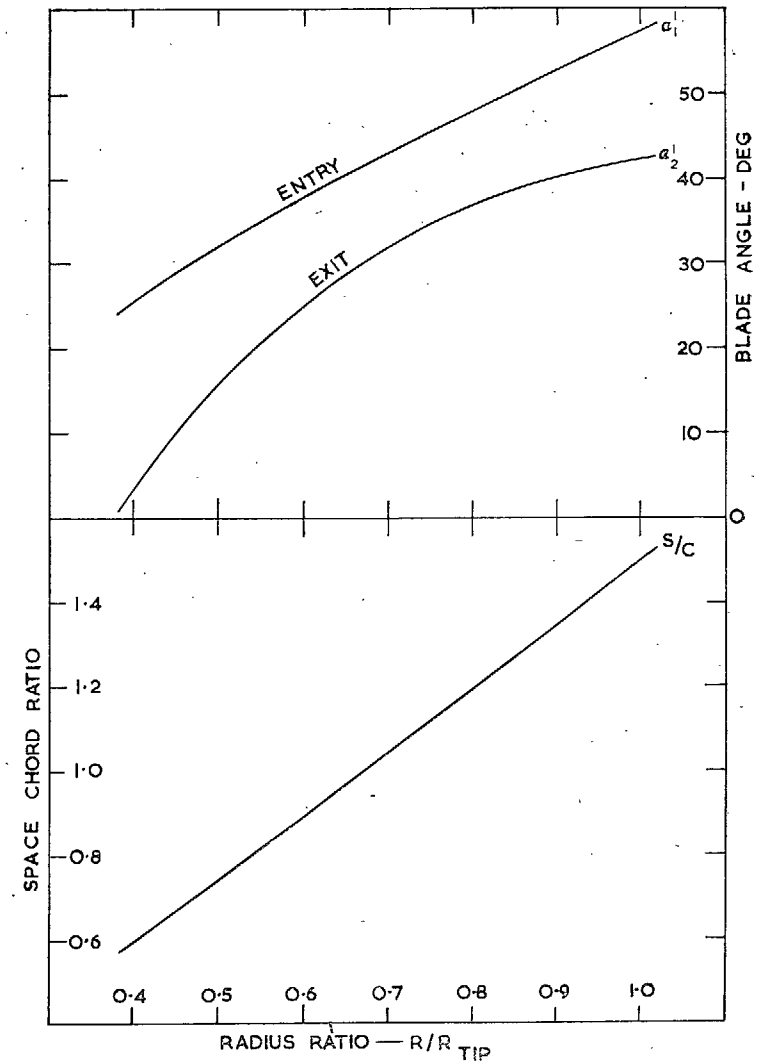

FIG. 3. Two-stage rig—rotor blading.

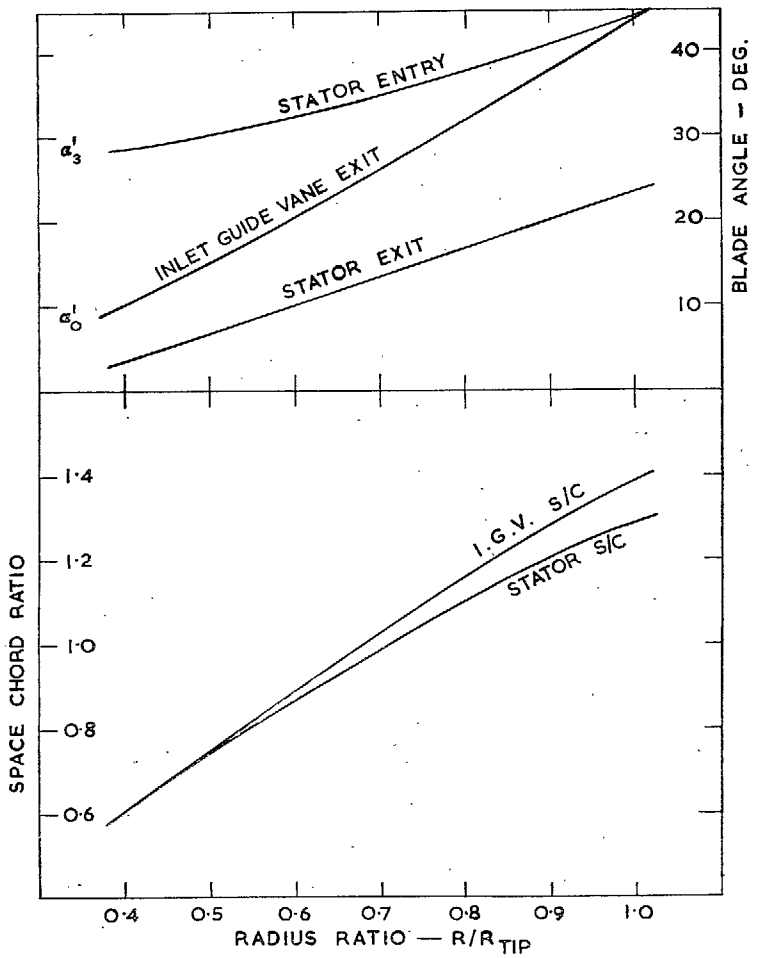

FIG. 4. Two-stage rig—inlet guide vane and stator blading.

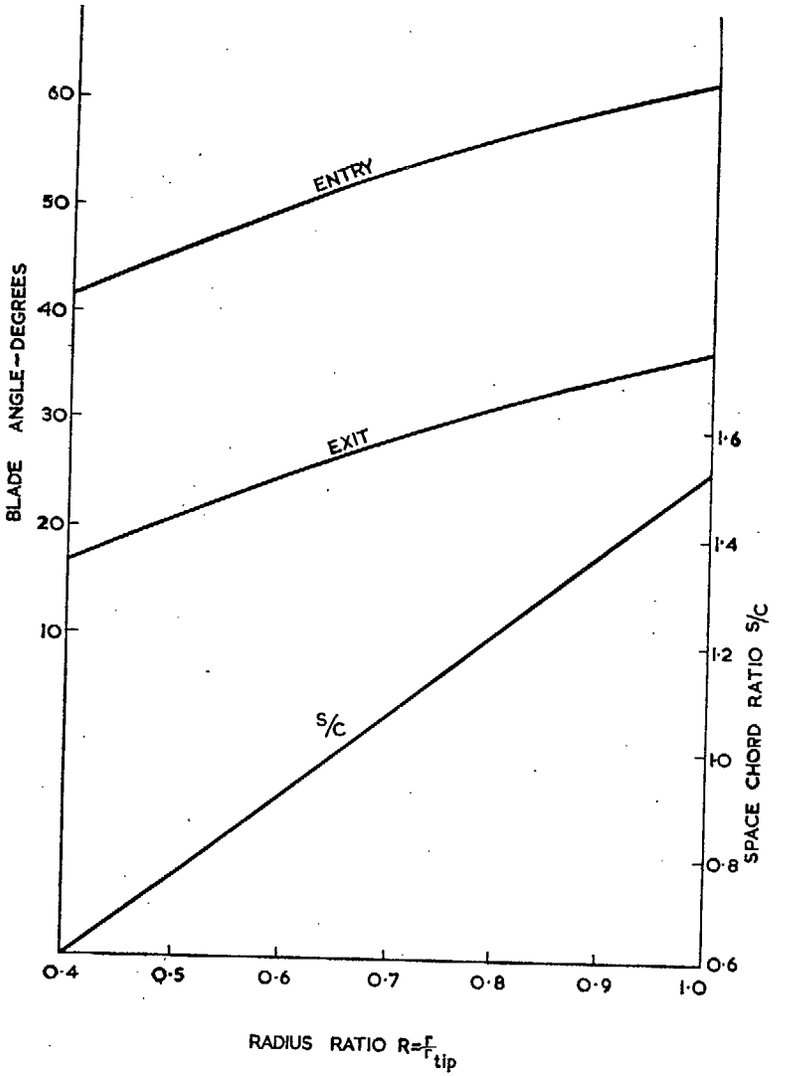

FIG. 5. Model stage—rotor blading.

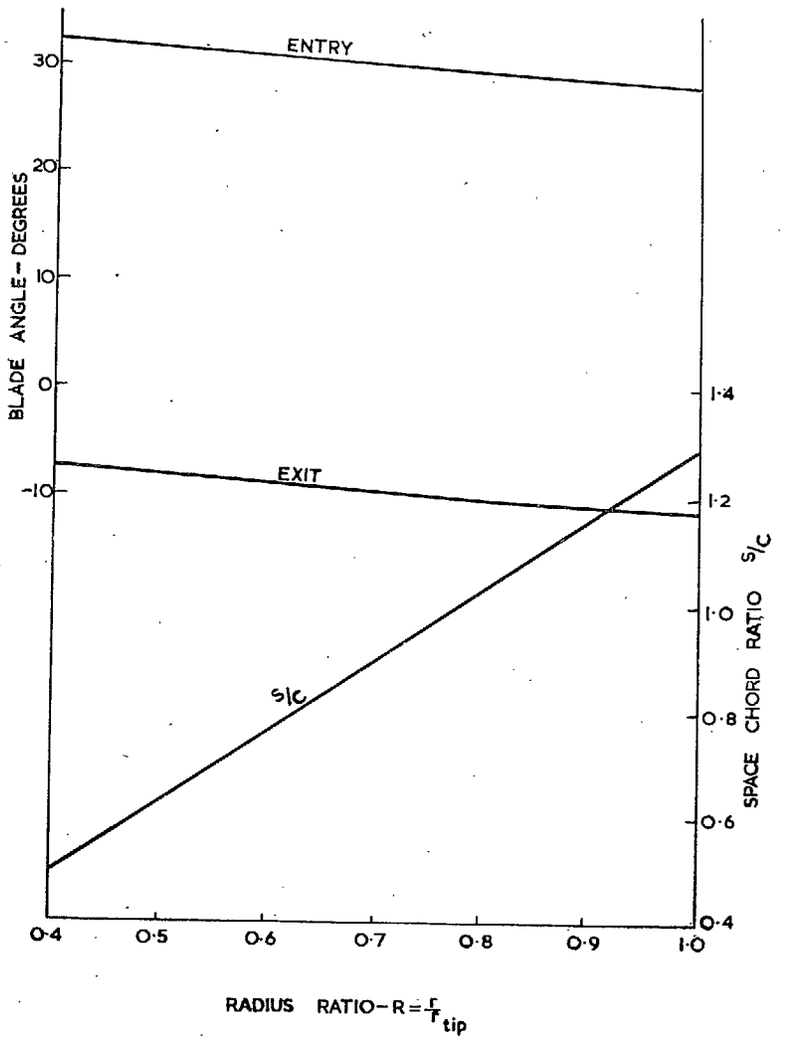

FIG. 6. Model stage—stator blading.

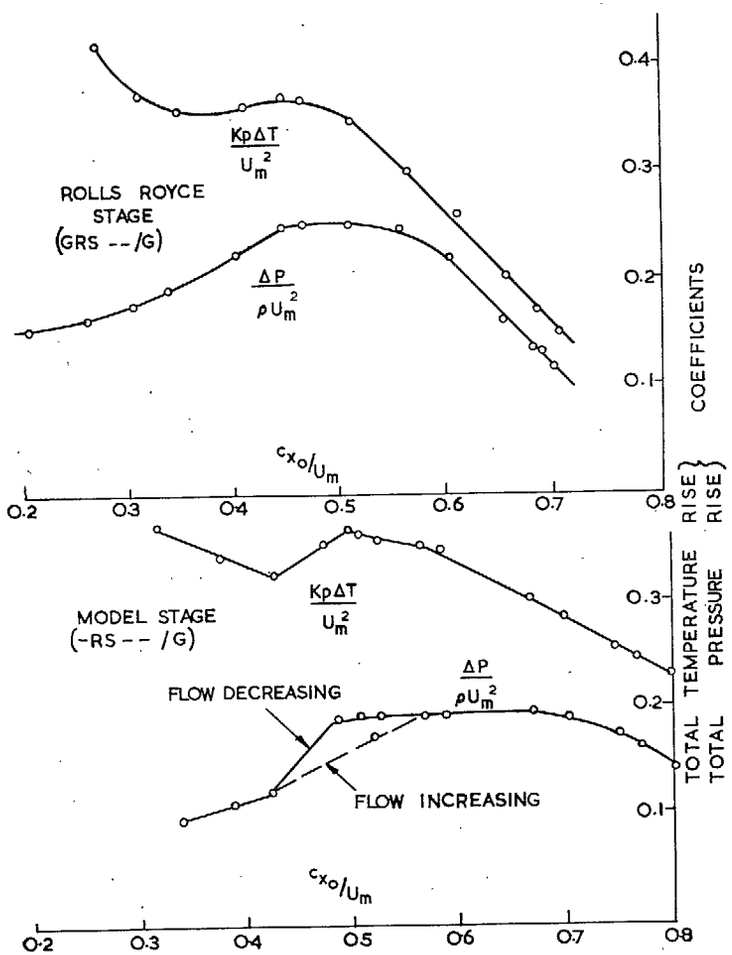

FIG. 7. Single-stage characteristics.

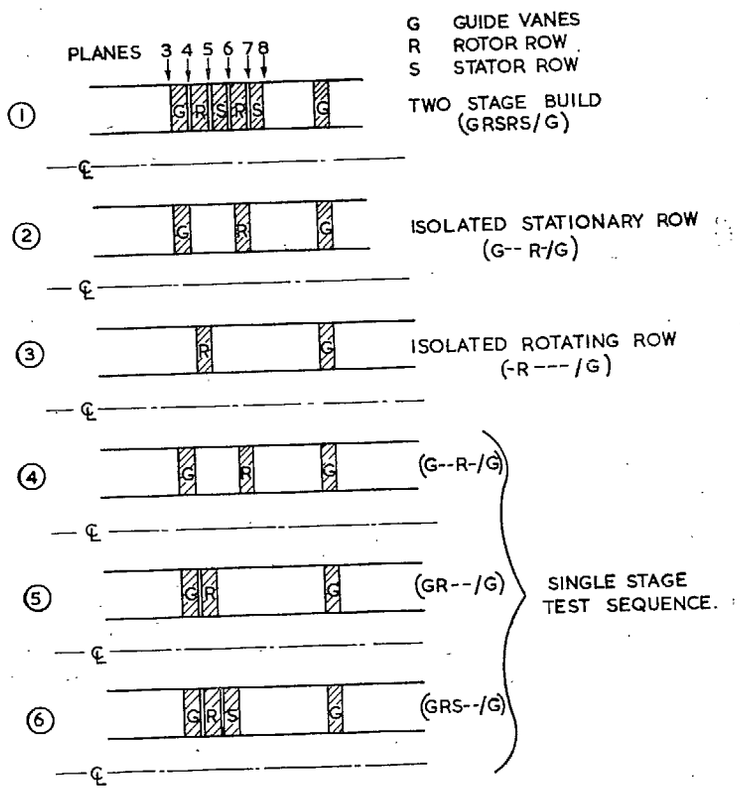

FIG. 8. Rolls-Royce compressor-stage builds (Diagrammatic).

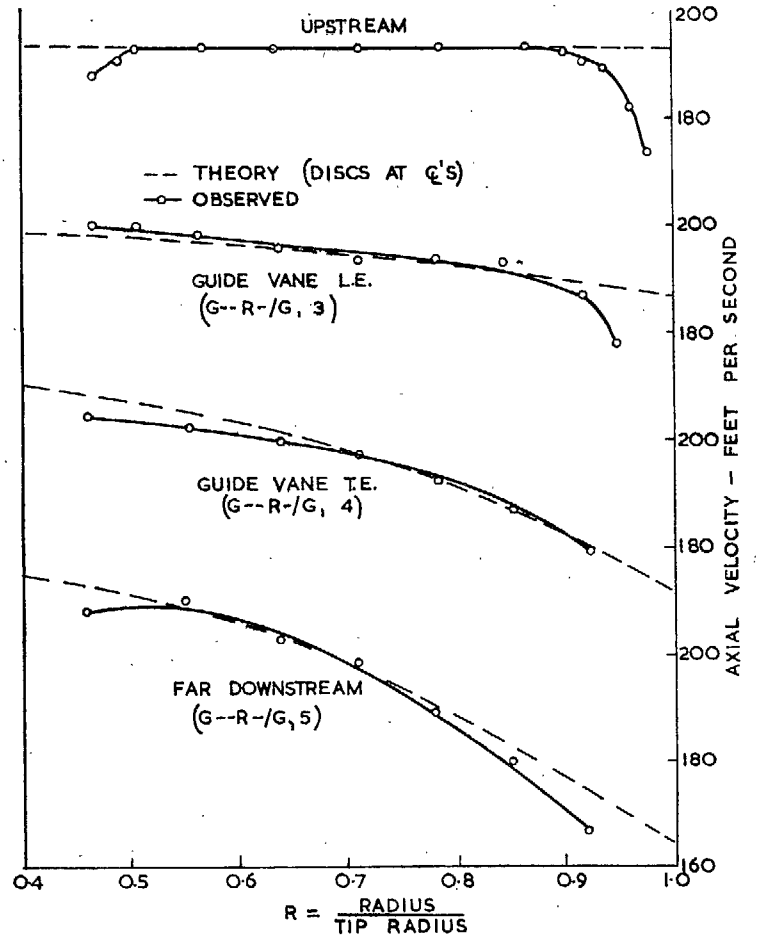

FIG. 9. Axial-velocity profiles (Rolls-Royce stage, stationary row. $C_{x1}/U_m = 0{\cdot}670$).

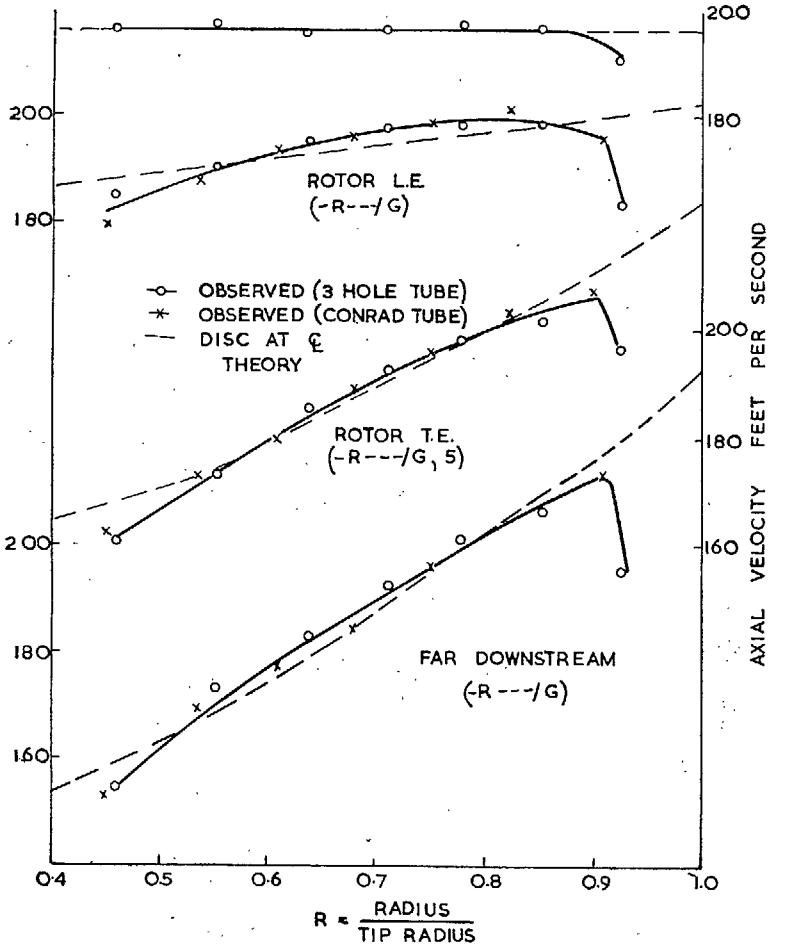

FIG. 10. Axial-velocity profiles (Rolls-Royce stage, rotating row $C_{x1}/U_m = 0{\cdot}670$).

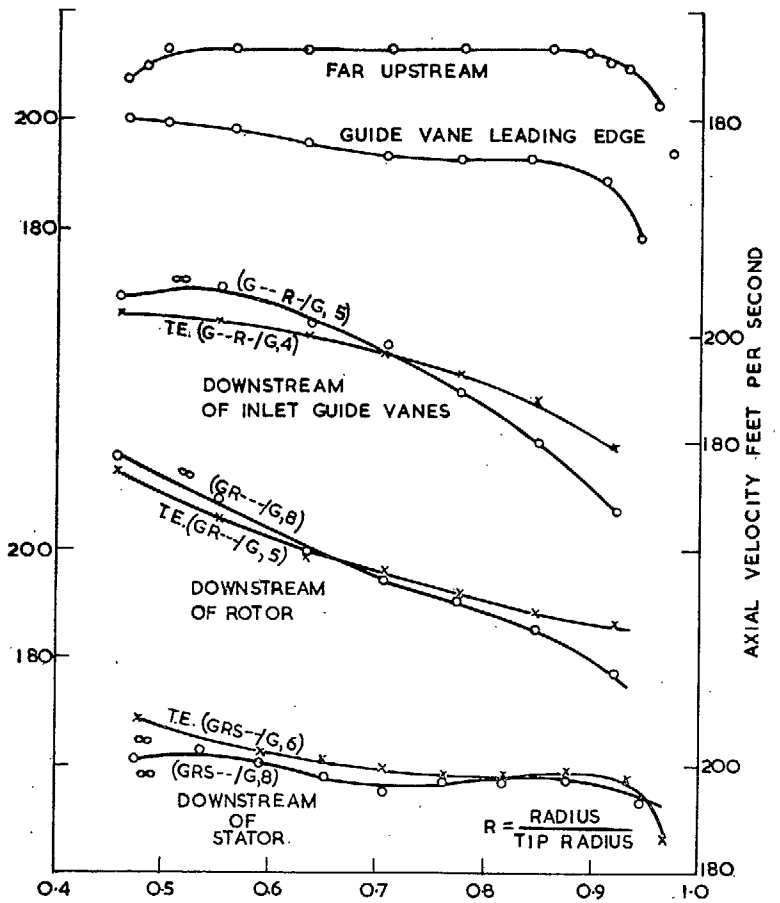

FIG. 11. Axial-velocity profile (Rolls-Royce stage—Decay effects —Observed. $C_{x1}/U_m = 0{\cdot}670$).

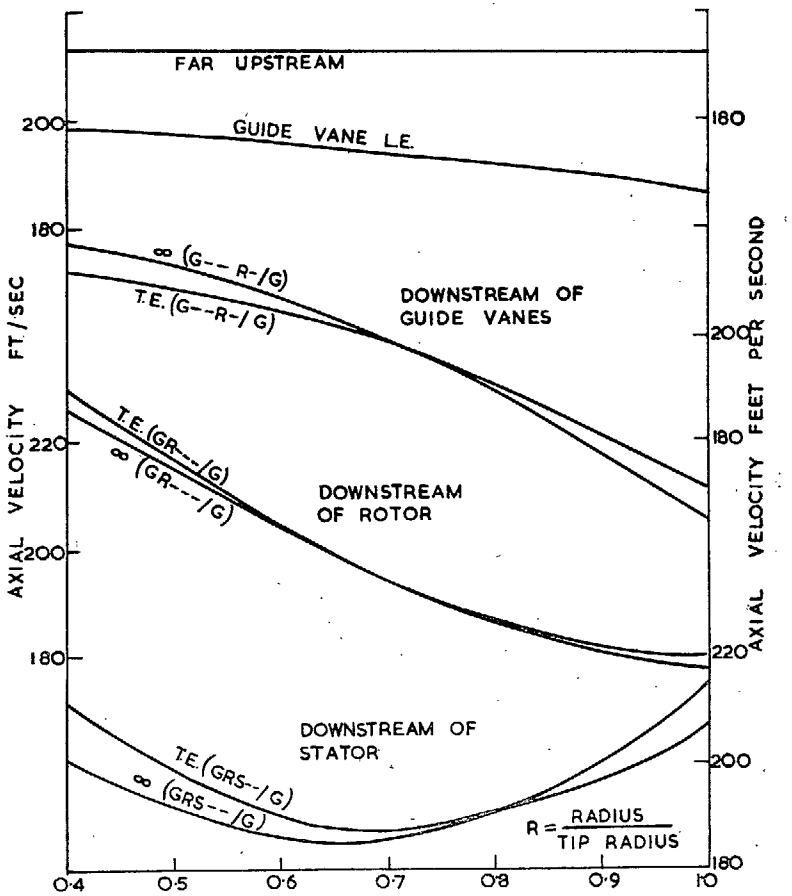

FIG. 12. Axial-velocity profiles (Rolls-Royce stage—Decay effects —Predicted. Discs at centres of pressure. $C_{x1}/U_m = 0{\cdot}670$).

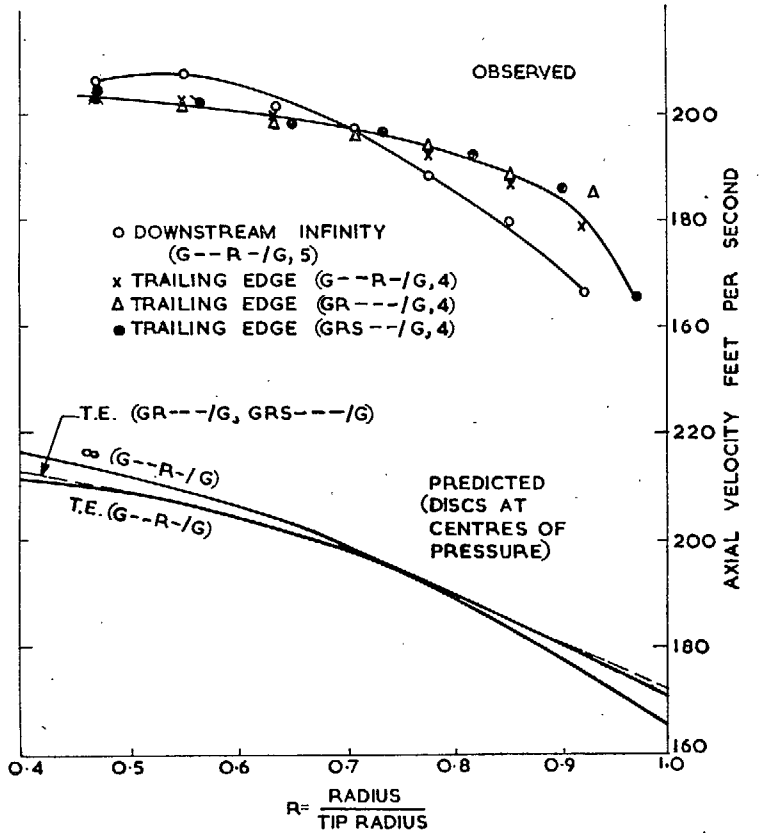

FIG. 13. Axial-velocity profiles (Rolls-Royce stage—Interference effects downstream of guide vanes. $C_{x1}/U_m = 0{\cdot}670$).

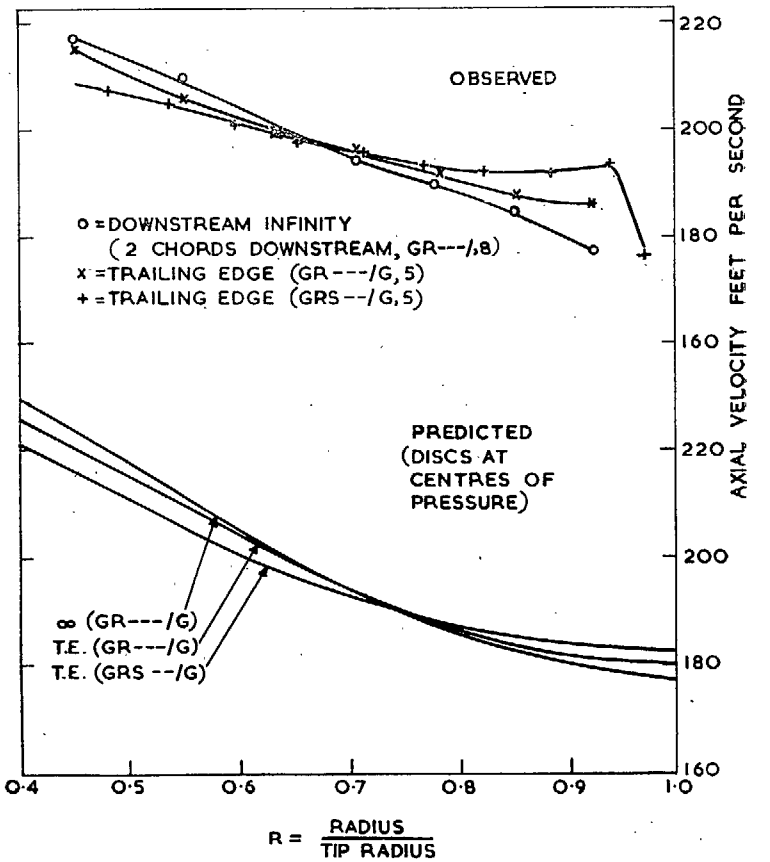

FIG. 14. Axial-velocity profiles (Rolls-Royce stage—Interference effects downstream of rotor. $C_{x1}/U_m = 0{\cdot}670$).

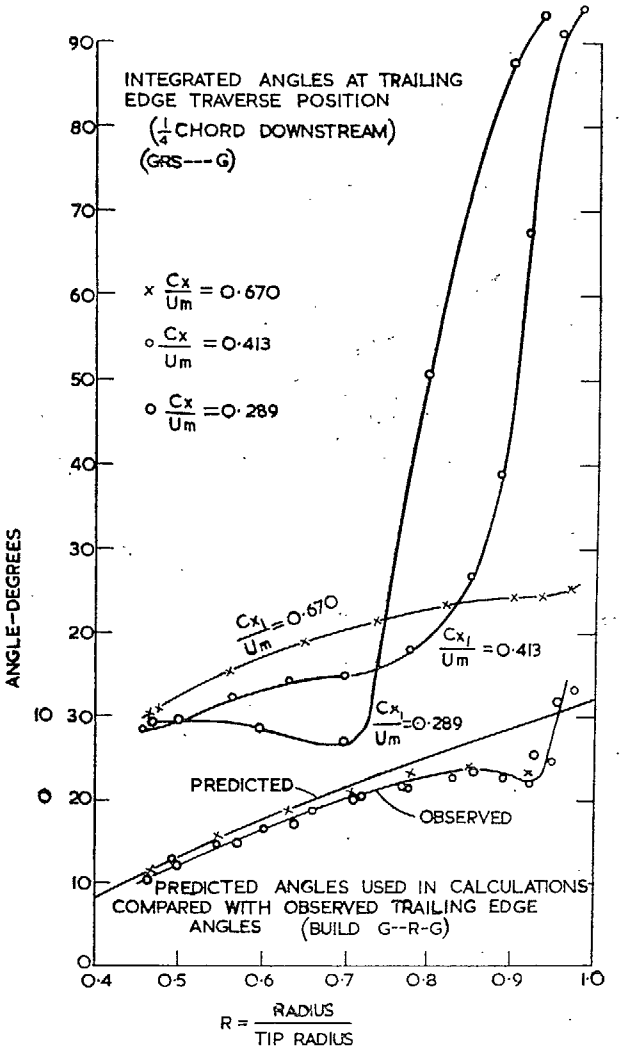

FIG. 15. Air angle downstream of guide vanes.

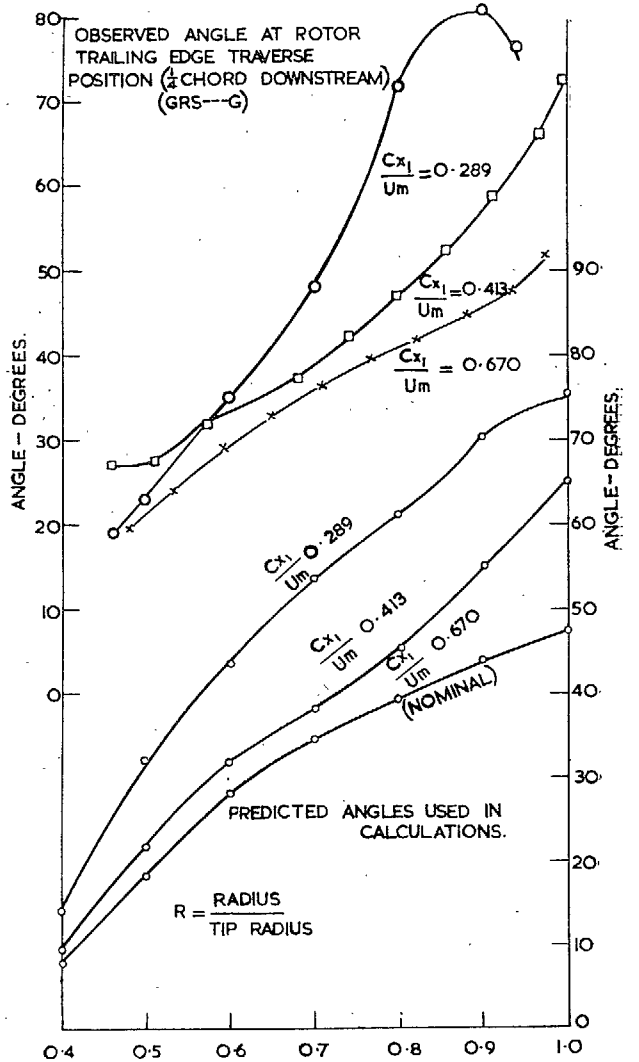

FIG. 16. Air angles (relative to rotor) downstream of rotor.

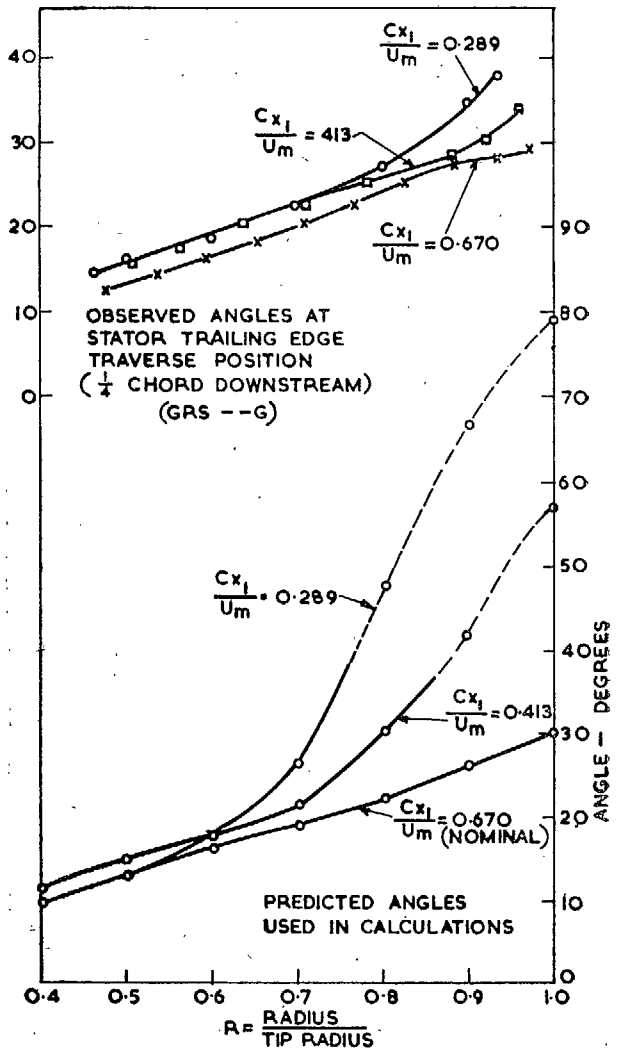

FIG. 17. Air angles downstream of stator.

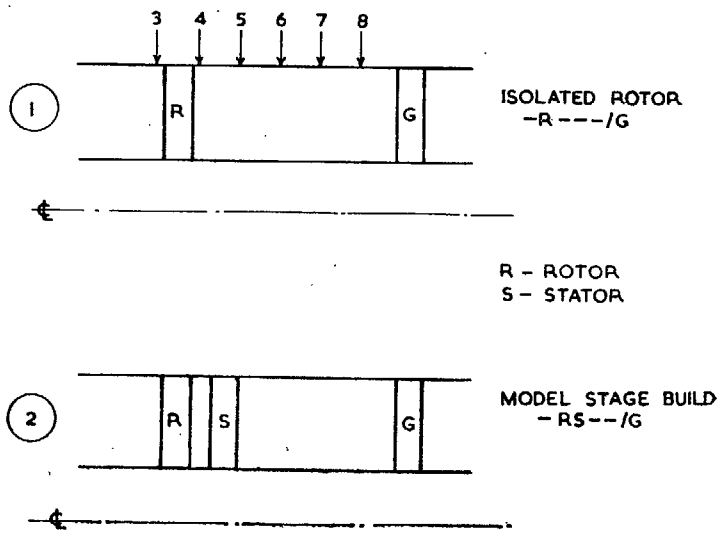

FIG. 18. Model stage. Compressor builds (Diagrammatic).

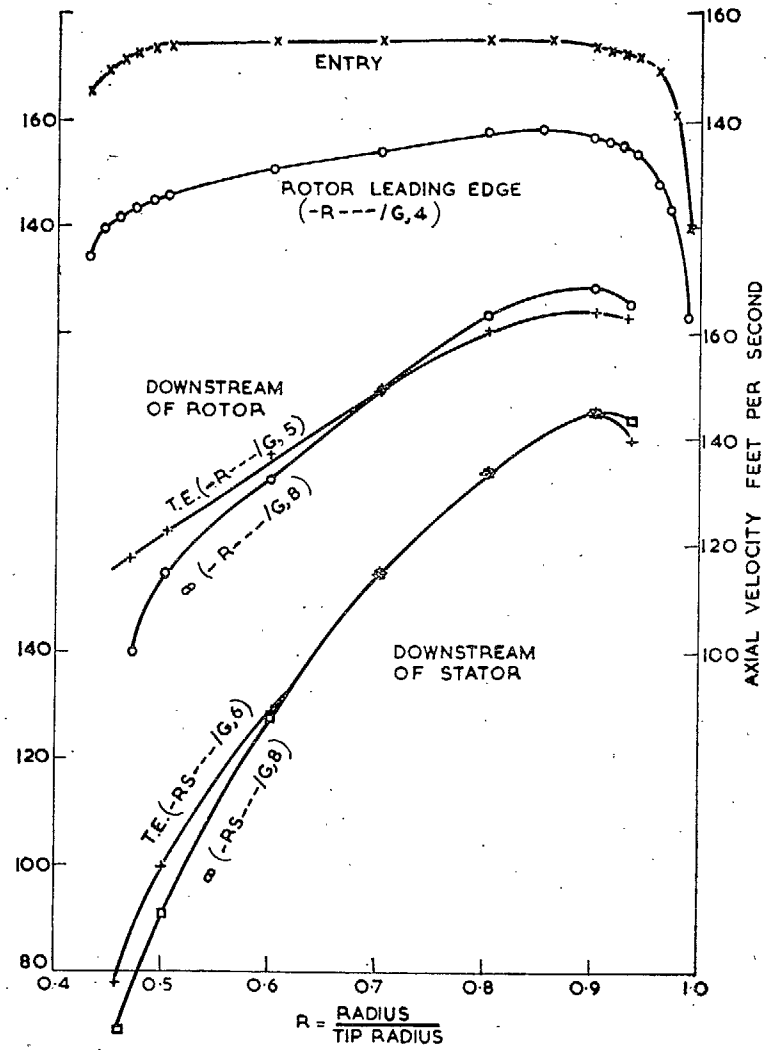

FIG. 19. Axial-velocity profiles (Model stage—Decay effects —Observed. $C_{x1}/_m U = 0{\cdot}720$).

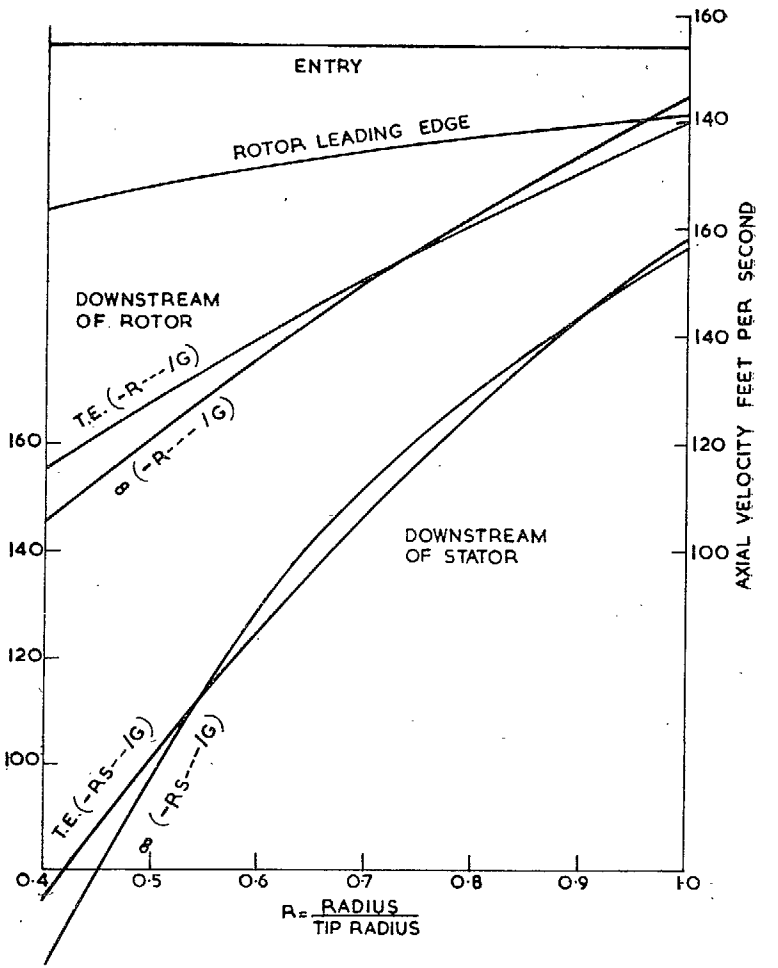

FIG. 20. Axial-velocity profiles (Model stage—Decay effects —Predicted. Discs at centre of pressure. $C_{x1}/U_m = 0{\cdot}720$).

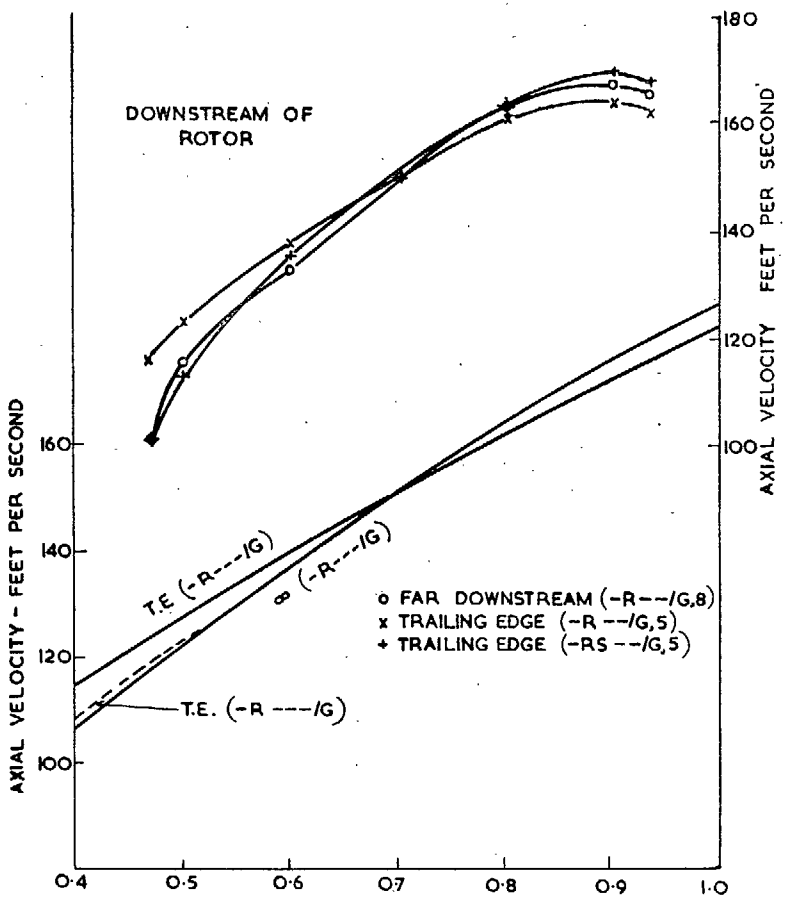

FIG. 21. Axial-velocity profiles (Model stage—Interference effects. $C_{x1}/_{m}U = 0{\cdot}720$).

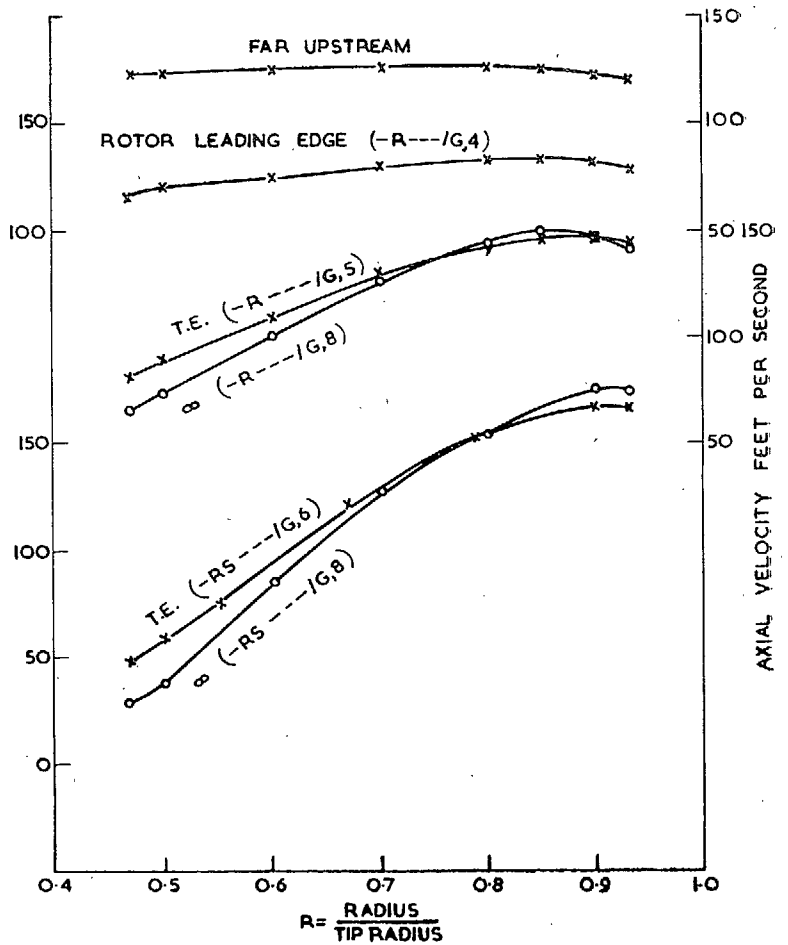

FIG. 22. Axial-velocity profiles (Model stage—Decay effects —Observed. $C_{x1}/U_m = 0{\cdot}585$).

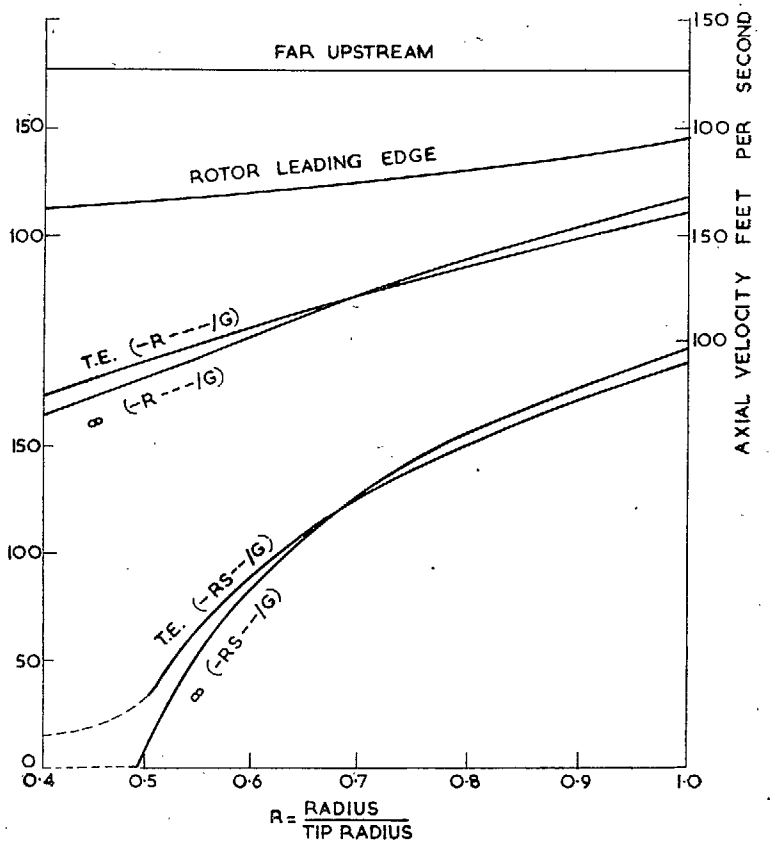

FIG. 23. Axial-velocity profiles (Model stage—Decay effects —Predicted. Discs at centres of pressure. $C_{x1}/U_m = 0{\cdot}585$)

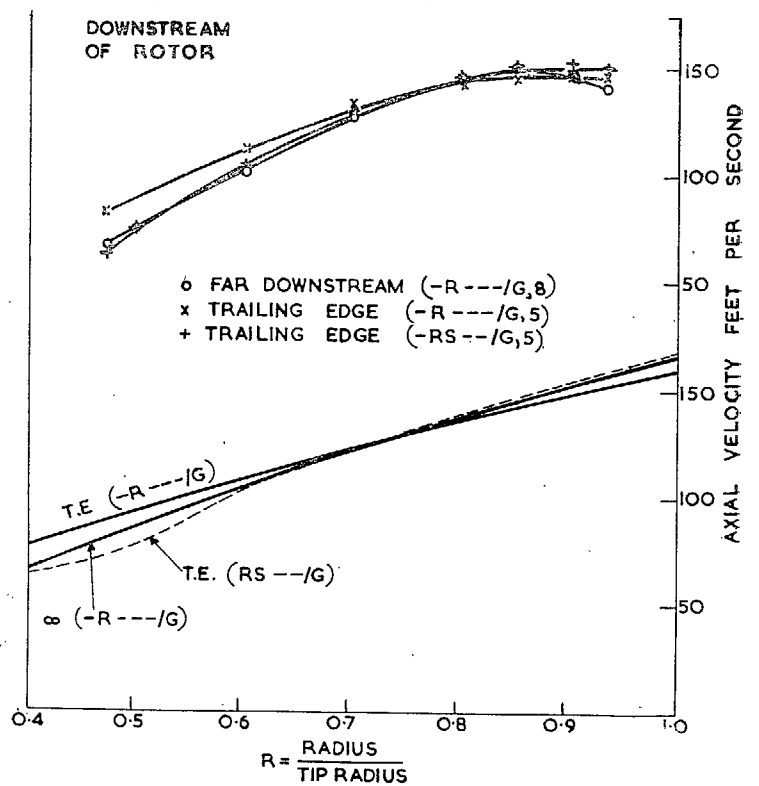

FIG. 24. Axial-velocity profiles (Model stage—Interference effects. $C_{x1}/U_m = 0{\cdot}585$).

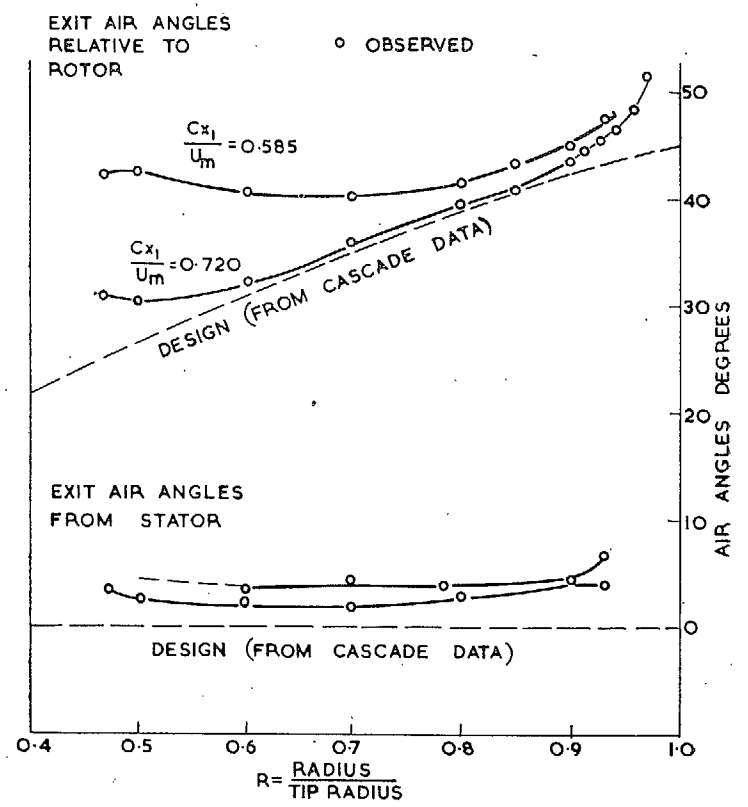

FIG. 25. Model stage—air angles.

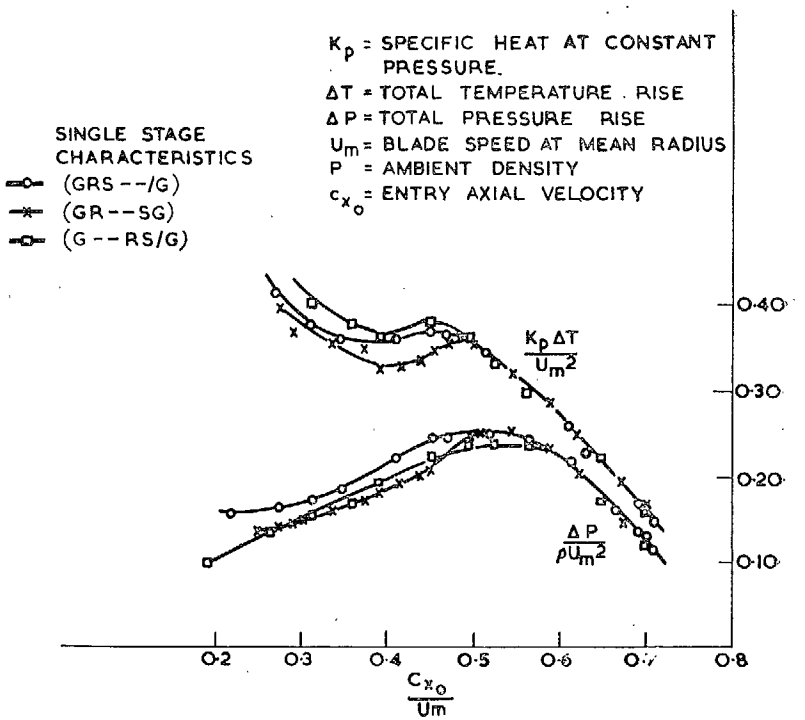

FIG. 26. Rolls-Royce compressor stage.

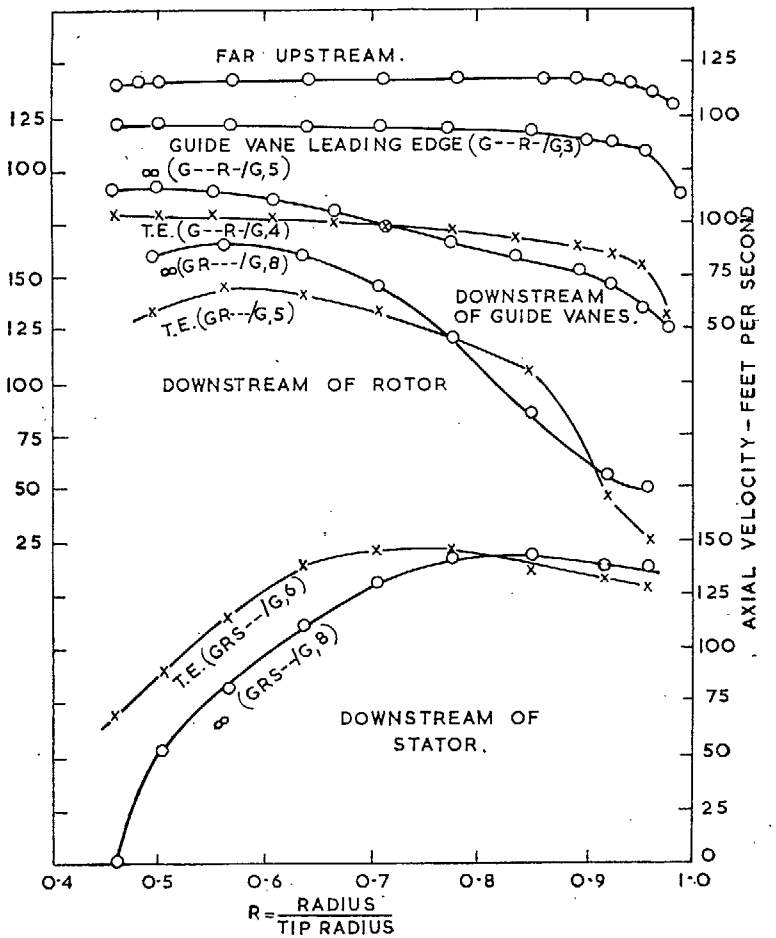

FIG. 27. Axial-velocity profiles (Rolls-Royce stage—Decay effects —Observed. $C_{x1}/U_m = 0{\cdot}413$.)

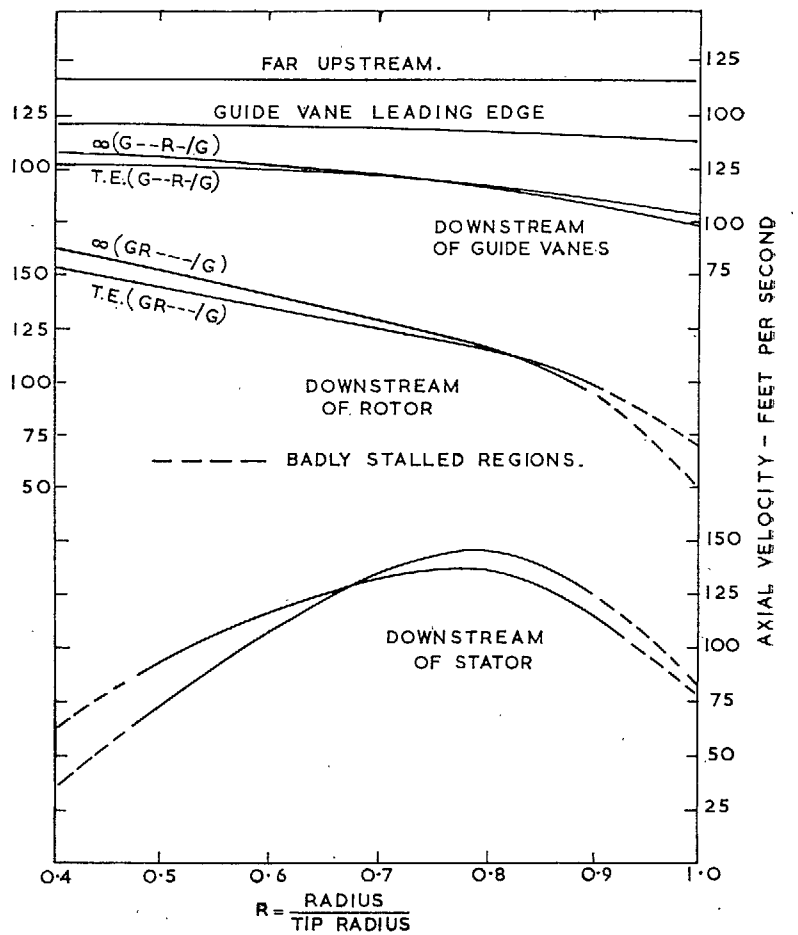

FIG. 28. Axial-velocity profiles (Rolls-Royce stage—Decay effects —Predicted. Discs at centre-lines. $C_{x1}/U_m = 0{\cdot}413$).

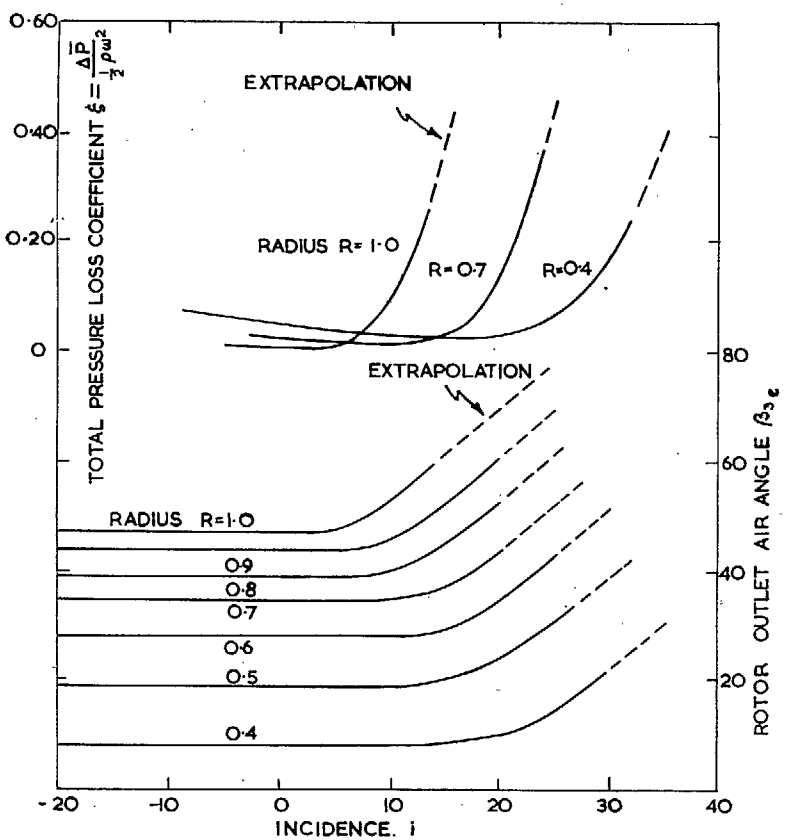

FIG. 29. Rolls-Royce compressor stage. Cascade data for rotor (From Howell).

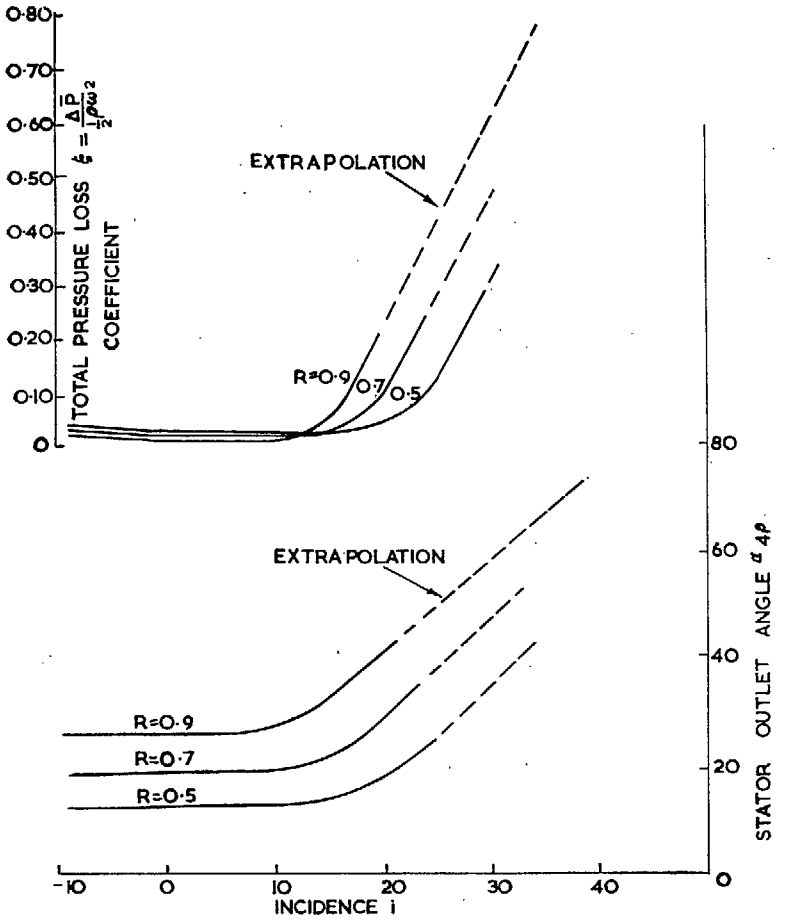

FIG. 30. Rolls-Royce compressor stage. Cascade data for stator (From Howell).

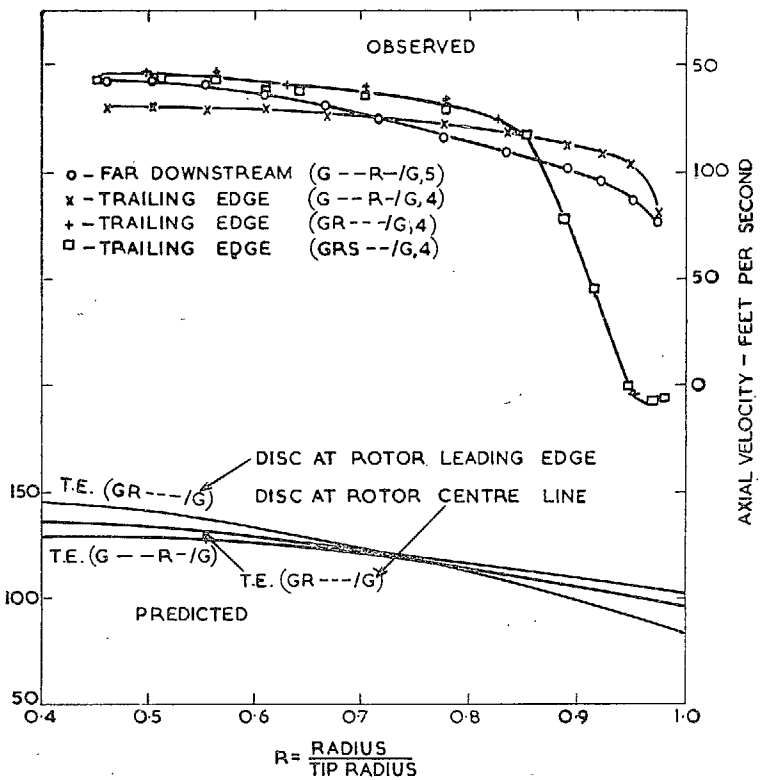

FIG. 31. Axial-velocity profiles (Rolls-Royce stage—Interference effects. $C_{x1}/U_m = 0{\cdot}413$).

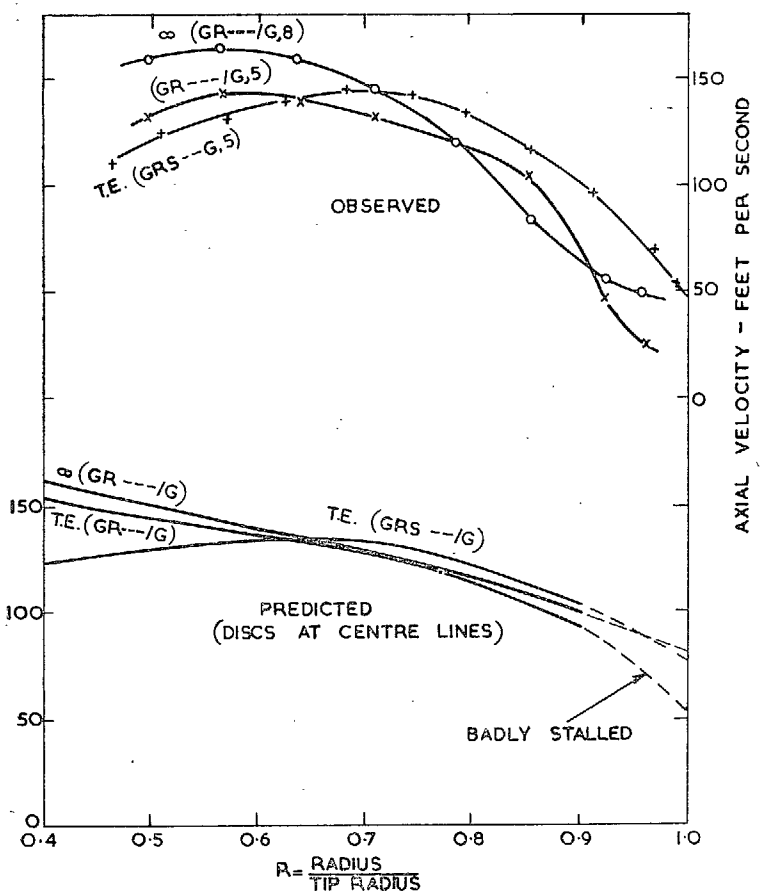

FIG. 32. Axial-velocity profiles (Rolls-Royce stage—Interference effects. $C_{x1}/U_m = 0{\cdot}413$).

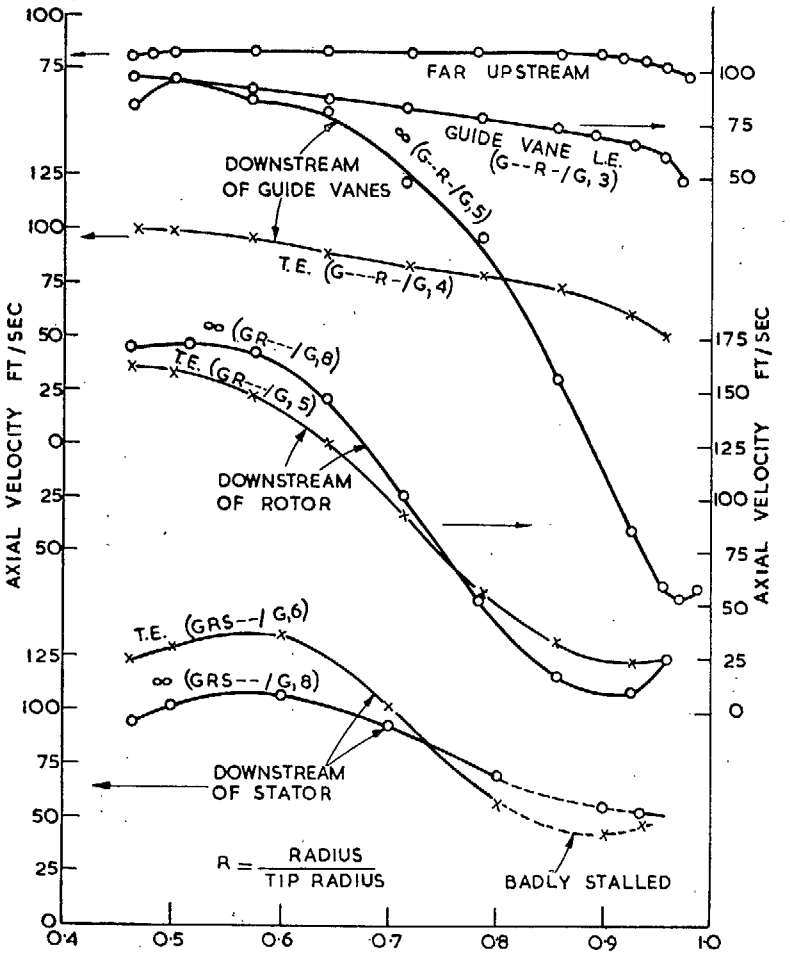

FIG. 33. Axial-velocity profiles (Rolls-Royce stage—Decay effects —Observed. $C_{x1}/U_m = 0{\cdot}289$).

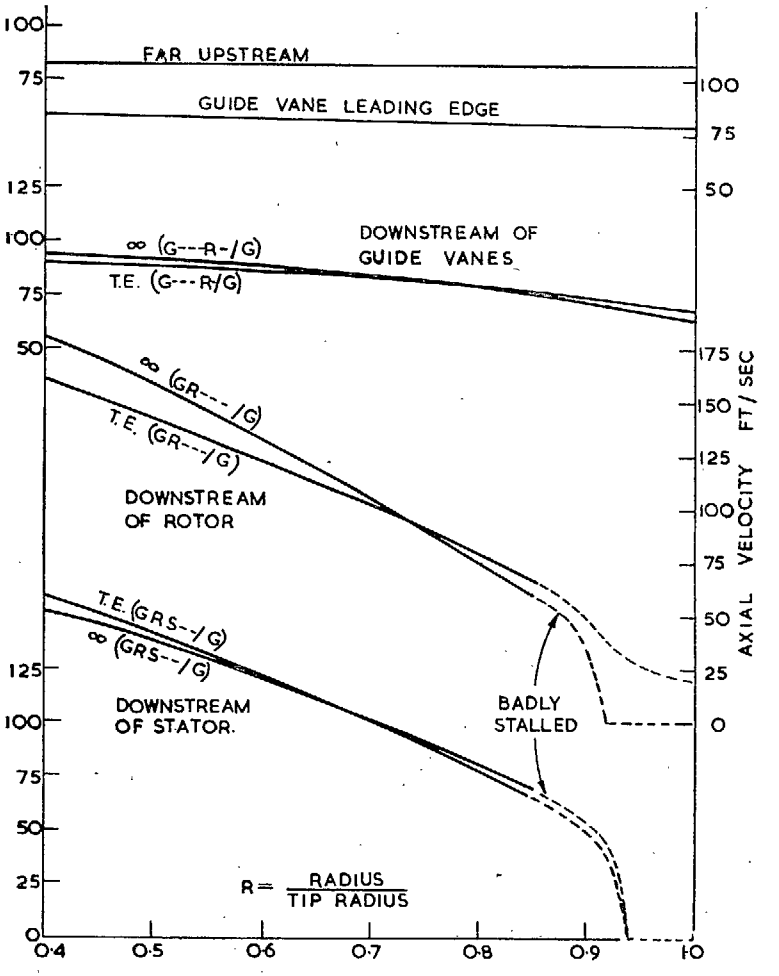

FIG. 34. Axial-velocity profiles (Rolls-Royce stage—Decay effects —Predicted discs at centre-line. $C_{x1}/U_m = 0{\cdot}289$).

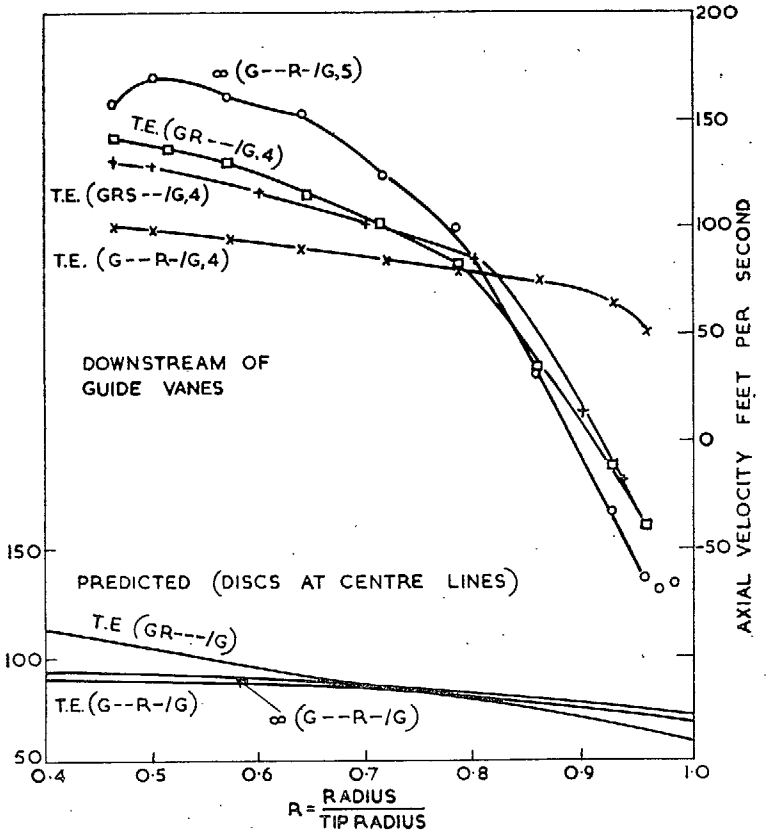

FIG. 35. Axial-velocity profiles (Rolls-Royce stage—Interference effects. $C_{x1}/U_m = 0{\cdot}289$).

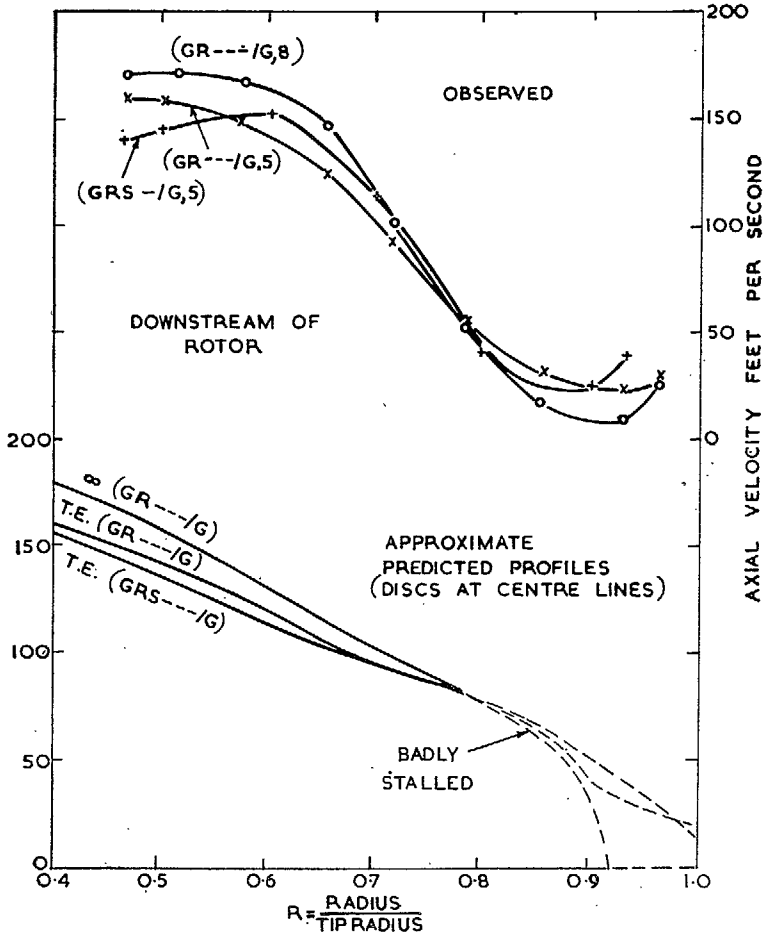

FIG. 36. Axial-velocity profiles (Rolls-Royce stage—Interference effects. $C_{x1}/U_m = 0{\cdot}289$).

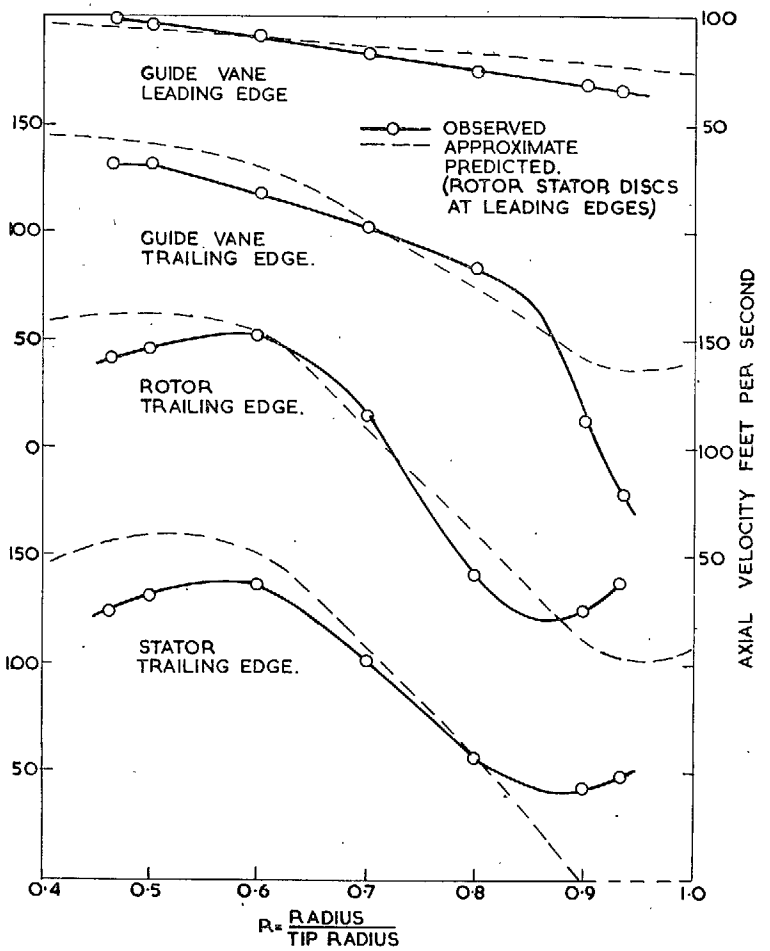

FIG. 37. Axial-velocity profiles (Rolls-Royce stage. $C_{x1}/U_m = 0 \cdot 289$).

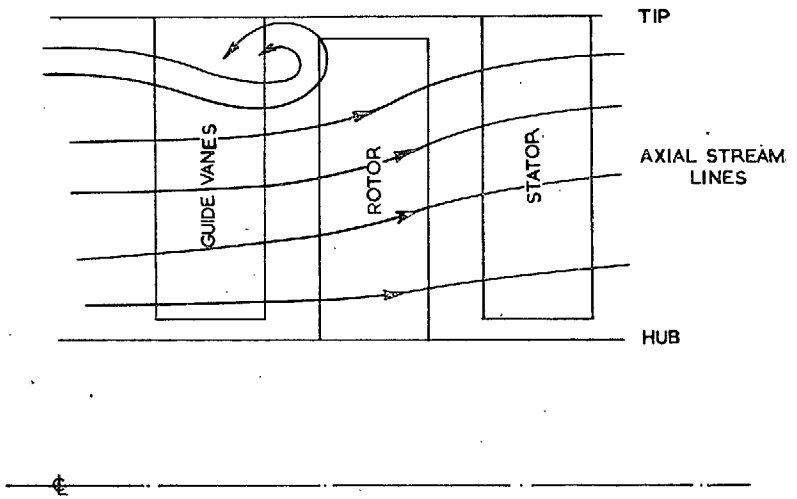

FIG. 38. Recirculation vortex at compressor tip.

J4379 W1.20/9036 K7 12/56 D&Co. 34/263

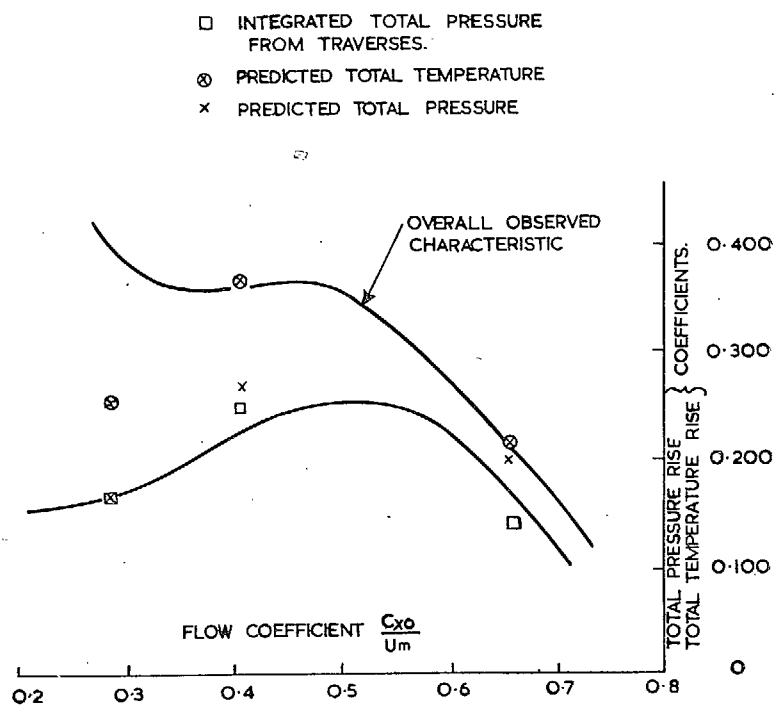

FIG. 39. Rolls-Royce stage characteristics.

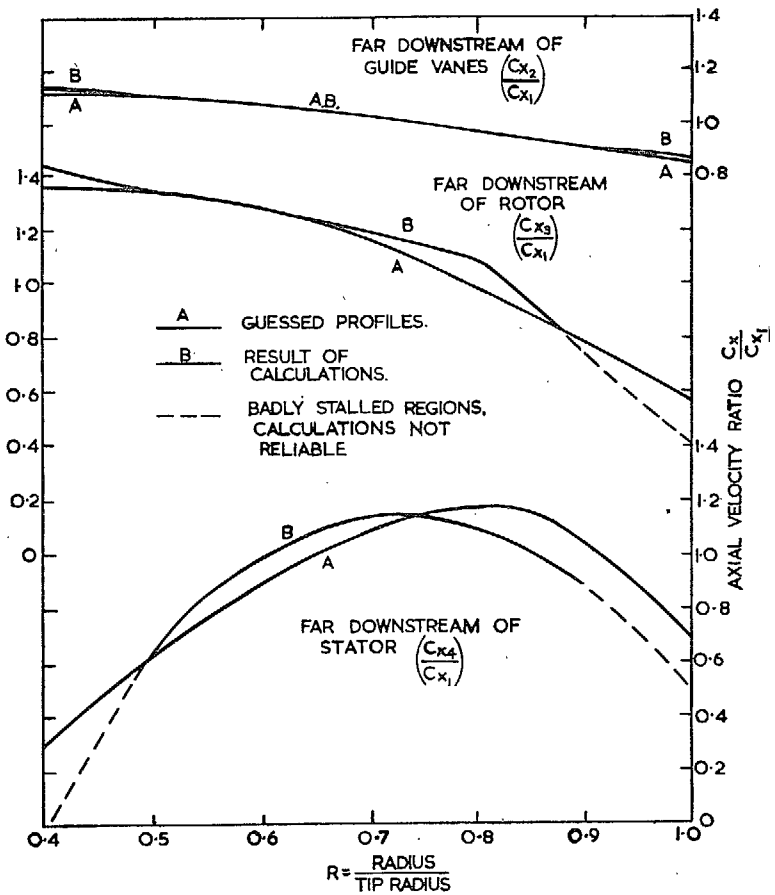

FIG. 40. Calculation of axial-velocity profiles. $C_{x1}/U_m = 0{\cdot}413$. (Entry C_{x1}).

PRINTED IN GREAT BRITAIN

Publications of the Aeronautical Research Council

ANNUAL TECHNICAL REPORTS OF THE AERONAUTICAL RESEARCH COUNCIL (BOUND VOLUMES)

1939 Vol. I. Aerodynamics General, Performance, Airscrews, Engines. 50*s*. (51*s*. 9*d*.)
Vol. II. Stability and Control, Flutter and Vibration, Instruments, Structures, Seaplanes, etc. 63*s*. (64*s*. 9*d*.)

1940 Aero and Hydrodynamics, Aerofoils, Airscrews, Engines, Flutter, Icing, Stability and Control, Structures, and a miscellaneous section. 50*s*. (51*s*. 9*d*.)

1941 Aero and Hydrodynamics, Aerofoils, Airscrews, Engines, Flutter, Stability and Control, Structures. 63*s*. (64*s*. 9*d*.)

1942 Vol. I. Aero and Hydrodynamics, Aerofoils, Airscrews, Engines. 75*s*. (76*s*. 9*d*.)
Vol. II. Noise, Parachutes, Stability and Control, Structures, Vibration, Wind Tunnels. 47*s*. 6*d*. (49*s*. 3*d*.)

1943 Vol. I. Aerodynamics, Aerofoils, Airscrews. 80*s*. (81*s*. 9*d*.)
Vol. II. Engines, Flutter, Materials, Parachutes, Performance, Stability and Control, Structures. 90*s*. (92*s*. 6*d*.)

1944 Vol. I. Aero and Hydrodynamics, Aerofoils, Aircraft, Airscrews, Controls. 84*s*. (86*s*. 3*d*.)
Vol. II. Flutter and Vibration, Materials, Miscellaneous, Navigation, Parachutes, Performance, Plates and Panels, Stability, Structures, Test Equipment, Wind Tunnels. 84*s*. (86*s*. 3*d*.)

1945 Vol. I. Aero and Hydrodynamics, Aerofoils. 130*s*. (132*s*. 6*d*.)
Vol. II. Aircraft, Airscrews, Controls. 130*s*. (132*s*. 6*d*.)
Vol. III. Flutter and Vibration, Instruments, Miscellaneous, Parachutes, Plates and Panels, Propulsion. 130*s* (132*s*. 3*d*.)
Vol. IV. Stability, Structures, Wind tunnels, Wind Tunnel Technique. 130*s*. (132*s*. 3*d*.)

ANNUAL REPORTS OF THE AERONAUTICAL RESEARCH COUNCIL—

1937 2*s*. (2*s*. 2*d*.) 1938 1*s*. 6*d*. (1*s*. 8*d*.) 1939–48 3*s*. (3*s*. 3*d*.)

INDEX TO ALL REPORTS AND MEMORANDA PUBLISHED IN THE ANNUAL TECHNICAL REPORTS, AND SEPARATELY—

April, 1950 – – – – – R. & M. No. 2600. 2*s*. 6*d*. (2*s*. 8*d*.)

AUTHOR INDEX TO ALL REPORTS AND MEMORANDA OF THE AERONAUTICAL RESEARCH COUNCIL—

1909–January, 1954 – – – R. & M. No. 2570. 15*s*. (15*s*. 6*d*.)

INDEXES TO THE TECHNICAL REPORTS OF THE AERONAUTICAL RESEARCH COUNCIL—

December 1, 1936 — June 30, 1939. R. & M. No. 1850. 1*s*. 3*d*. (1*s*. 5*d*.)
July 1, 1939 — June 30, 1945. – R. & M. No. 1950. 1*s*. (1*s*. 2*d*.)
July 1, 1945 — June 30, 1946. – R. & M. No. 2050. 1*s*. (1*s*. 2*d*.)
July 1, 1946 — December 31, 1946. R. & M. No. 2150. 1*s*. 3*d*. (1*s*. 5*d*.)
January 1, 1947 — June 30, 1947. – R. & M. No. 2250. 1*s*. 3*d*. (1*s*. 5*d*.)

PUBLISHED REPORTS AND MEMORANDA OF THE AERONAUTICAL RESEARCH COUNCIL—

Between Nos. 2251–2349. – – R. & M. No. 2350. 1*s*. 9*d*. (1*s*. 11*d*.)
Between Nos. 2351–2449. – – R. & M. No. 2450. 2*s*. (2*s*. 2*d*.)
Between Nos. 2451–2549. – – R. & M. No. 2550. 2*s*. 6*d*. (2*s*. 8*d*.)
Between Nos. 2551–2649. – – R. & M. No. 2650. 2*s*. 6*d*. (2*s*. 8*d*.)

Prices in brackets include postage

HER MAJESTY'S STATIONERY OFFICE

York House, Kingsway, London W.C.2; 423 Oxford Street, London W.1;
13a Castle Street, Edinburgh 2; 39 King Street, Manchester 2; 2 Edmund Street, Birmingham 3; 109 St. Mary Street, Cardiff; Tower Lane, Bristol 1; 80 Chichester Street, Belfast, *or through any bookseller*

S.O. Code No. 23-3031